PCCP
Physical Chemistry Chemical Physics

# Accepted Manuscript

This article can be cited before page numbers have been issued, to do this please use: J. J. Gutierrez Moreno, M. Fronzi, P. Lovera, A. O'Riordan, M. Ford, W. Li and M. Nolan, *Phys. Chem. Chem. Phys.*, 2019, DOI: 10.1039/C9CP04506F.




ROYAL SOCIETY OF CHEMISTRY

rsc.li/pccp

View Article Online
DOI: 10.1039/C9CP04506F

ARTICLE

# Structure, stability and water adsorption on ultra-thin $TiO_2$ supported on TiN

José Julio Gutiérrez Moreno [a,b,c *], Marco Fronzi [d,e], Pierre Lovera [c], Alan O'Riordan [c], Michael J. Ford [e], Wenjin Li [a §], Michael Nolan [c†].

Interfacial metal-oxide systems with ultra-thin oxide layers are of high interest for their use in catalysis. The chemical activity of ultra-thin metal-oxide layers can be substantially enhanced compared to interfacial models with thicker oxide. In this study, we present a Density Functional Theory (DFT) investigation of the structure of ultra-thin rutile layers (one and two $TiO_2$ layers) supported on TiN and the stability of water on these interfacial structures. The rutile layers are stabilized on the TiN surface through the formation of interfacial Ti–O bonds. Charge transfer from the TiN substrate leads to the formation of reduced $Ti^{3+}$ cations in $TiO_2$. The concentration of $Ti^{3+}$ is proportionally higher in the ultra-thin oxide, compared to interfacial models with thicker oxide layers. The structure of the one-layer oxide slab is strongly distorted at the interface while the thicker $TiO_2$ layer preserves the rutile structure. The energy cost for the formation of a single O vacancy in the one-layer oxide slab is only 0.5 eV with respect to the ideal interface. For the two-layer oxide slab, the introduction of several vacancies in an already non-stoichiometric system becomes progressively more favourable, which indicates the stability of the highly defective interfaces. Isolated water molecules dissociate when adsorbed at the $TiO_2$ layers. At higher coverages, the preference is for molecular water adsorption. Our ab-initio thermodynamics calculations show the fully water covered stoichiometric models as the most stable structure at typical ambient conditions. This behaviour is similar to that observed on thicker oxide in $TiO_2$-TiN interfaces or pure $TiO_2$ surfaces. In contrast, interfacial models with multiple vacancies are most stable at low (reducing) oxygen chemical potential values. The high concentration on reduced $Ti^{3+}$ introduces significant distortions in the O-defective slab. Whereas, a water monolayer adsorbs dissociatively on the highly distorted 2-layer $TiO_{1.75}$-TiN interface, where the $Ti^{3+}$ states lying above the top of the valence band contribute to a significant reduction of the energy gap compared to the stoichiometric $TiO_2$-TiN model. Our results provide a guide for the design of novel interfacial systems containing ultra-thin $TiO_2$ with potential application as photocatalytic water splitting devices.

## 1. Introduction

Titanium nitride (TiN) protective coatings are used in multiple technologies and applications including biomedical and surgical instruments, automotive and aerospace parts and sporting goods [1-4]. The widespread use of TiN comes from its capacity to enhance the hardness, resistance to corrosion and biocompatibility of other materials [3-6]. TiN is also used in microelectronic devices, due to its good conductivity and significant plasmonic performance [7] while it is a potential anti-biofouling coating for detectors that are designed to be exposed to harsh environments [6, 8, 9]. TiN films can be fabricated by widely-used deposition techniques [10] including magnetron sputtering [5, 11], ion-beam sputtering (IBS) [12], physical vapour deposition (PVD) [13-16], chemical vapour deposition (CVD) [17-19] or atomic layer deposition (ALD) [20, 21].

TiN can be oxidised to produce a $TiO_2$ layer or scale when it is exposed to high temperatures or after long exposure times at ambient conditions [22-27]. The formation of a thin $TiO_x$ layer on the nitride surface can deteriorate the adherence of the coating, which will affect the mechanical properties and resistivity to corrosion [25, 28, 29]. However, there are other applications of such an interfacial system in which the growth of ultra-thin $TiO_2$ films is precisely controlled and one example is in catalysis, where ultra-thin films can show potential for $H_2O$ splitting [30, 31], $CO_2$ reduction [32] or fixation of $N_2$ to $NH_3$ [33]. In bulk $TiO_2$, doping or defect formation is needed to produce reduced $Ti^{3+}$ sites, which can be difficult to control. By contrast, we have

[a.] Institute for Advanced Study, Shenzhen University, Shenzhen 518060, China.
[b.] Key Laboratory of Optoelectronic Devices and Systems of Ministry of Education and Guangdong Province, College of Physics and Optoelectronic Engineering, Shenzhen University, Shenzhen 518060, China.
[c.] Tyndall National Institute, University College Cork. Lee Maltings, Dyke Parade, Cork, T12 R5CP, Ireland.
[d.] International Research Centre for Renewable Energy, State Key Laboratory of Multiphase Flow in Power Engineering, Xi'an Jiaotong University, Xi'an 710049, Shaanxi, China
[e.] School of Mathematical and Physical Sciences, University of Technology Sydney, P.O. Box 123, Broadway, Sydney, New South Wales 2007, AustraliaAddress here.

Email: *juliogutierrez@szu.edu.cn, §liwenjin@szu.edu.cn, †michael.nolan@tyndall.ie

Electronic Supplementary Information (ESI) available: Structure of Ti defect in 1-layer thick rutile $TiO_2$ (110)–TiN (100) interface, Structures of single water adsorbed at 1-layer thick O-defective $TiO_2$ -TiN interfaces; Structure of dissociated water monolayer on perfect 2-layer thick rutile (110) $TiO_2$ -TiN interface; Adsorption energy and bond distances for water on rutile $TiO_2$ (110) – TiN (100) interfaces; Partial Density of States (PDOS) of pristine and water covered 1-layer thick O-defective $TiO_2$-TiN interfaces and 2-layer thick stochiometric and O-defective interfaces.

shown that in $TiO_2$-TiN interfaces, reduced $Ti^{3+}$ states in $TiO_2$ are naturally formed as a result of charge transfer from TiN to $TiO_2$. The well-known reduced $Ti^{3+}$ states lie in the middle of the $TiO_2$ energy gap. Thus, the controlled growth of $TiO_2$ on TiN could be further used for tuning the $TiO_2$ optical bandgap by oxide-nitride interaction, potentially leading to an optimized catalytic performance under visible light [34-36].

The oxidation of TiN is a complex process and the structure of the resulting oxide will be highly dependent on the temperature and the thickness of the oxide layer. Ab-initio molecular dynamics simulations [37] showed that at high temperatures, an ordered and non-defective crystalline $TiO_2$ structure tends to form on the TiN surface. The difficulty in adsorbing oxygen after the formation of $TiO_2$ layers can prevent further TiN oxidation. At low temperatures, defects can remain trapped inside the interface [37]. From experiments, it is observed that TiN deposited by CVD on Si (100) forms a uniform film with stoichiometric composition and predominance of (200) out-of-plane orientation at deposition temperatures in the range of 400-700 ºC [38]. The epitaxial growth of $TiO_2$ on TiN leads to the formation of rutile $TiO_2$ (110) with the presence of an interfacial oxynitride ($TiN_xO_y$) transition layer [39].

In a previous publication [40], we used Hubbard corrected density functional theory (DFT+U) to study the structure and electronic properties of rutile $TiO_2$ (110)–TiN (100) interfaces, using a sufficiently thick rutile (110) slab model to ensure that the $TiO_2$ is close to bulk-like. We have found that in the rutile (110)–TiN interface system defects such as Ti vacancies in TiN, O vacancies in $TiO_2$ or interdiffusion of O and N atoms within the interface may be present. We observed the formation of $Ti^{3+}$ cations, preferentially located in the interface region, which originate from charge transfer to $TiO_2$ upon interface formation or from the introduction of O vacancies in non-stoichiometric systems.

$TiO_2$ is one of the most extensively investigated metal oxides [41-46] and the wettability of $TiO_2$ can be tuned by surface morphology modifications or UV irradiation enhancing the hydrophilic features of the surface for its use as antibiofouling or self-cleaning coating material [47-49]. The multitude of $TiO_2$ applications and the ubiquitous presence of water explains the great interest in studying the interaction of water with different $TiO_2$ surfaces [41, 50, 51]. Water adsorption on $TiO_2$ can be described either as molecular or dissociative; in the latter surface, hydroxyls result from the dissociation of $H_2O$ into OH + H [50, 52]. Most experimental works agree that water adsorbs molecularly at a pristine rutile (110) surface and dissociation may take place on site defects and step edges [41, 50, 53]. Nevertheless, there still remains some controversy from theoretical studies on water adsorption at pure $TiO_2$ and the results can be highly dependent on the simulation setup parameters, e.g. slab thickness, surface coverage or exchange-correlation functional [41].

When the oxide layer on TiN grows above a certain thickness, the resulting oxide can be considered as pure $TiO_2$ and the surface morphology will not be affected by the substrate material. In our previous work [54], we showed that when water is adsorbed on the rutile surface of $TiO_2$–TiN interfaces with a 4 O-Ti-O tri-layer thick oxide (11.10 Å), this behaves similarly to pure $TiO_2$. We found that at ambient $O_2$ and $H_2O$ pressures the interface is fully covered with molecular water. Isolated water molecules tend to dissociate on the rutile surface, although these are stable only at very low $H_2O$ pressures. These results are in line with a previous DFT study of water adsorption on pure $TiO_2$ [55].

The increasing interest in metal-oxide interfacial systems lies in the fact that the properties of the oxide can be significantly altered by the characteristics of the substrate and vice versa. This effect can be explained as a result of the lattice distortion that the oxide requires to match the substrate's lattice parameters combined with potential charge transfer that takes place in the metal-oxide interface. The film thickness is a critical factor that determines the catalytic activity of ultra-thin oxide films supported on a metal substrate. The chemical activity of a single metal-oxide monolayer deposited on a metallic substrate can be substantially enhanced compared to the bulk oxide's surface or interfacial models with extended oxide layers. [56] In ultra-thin oxides, the geometry distortions are usually more severe than in bulk-like oxide films, being also strongly affected by electronic hybridizations in the interfacial region. As an example, previous studies on single water molecule adsorption at ultra-thin MgO (100) supported on Ag (100) [56, 57] and Mo (100) [58] found enhanced water adsorption and reduced dissociation barriers on the interfacial systems when compared to the extended MgO (100) surface. This preference for dissociated water has its origin in the interfacial tensile strain that causes an expansion of the MgO lattice, which facilitates the dissociation of water. Charge-transfer effects are not considered as crucial [56, 58]. Nevertheless, theoretical studies on molecular adsorption at oxide-metal interfaces remain scarce.

As far as we are aware, the only first-principles study on water adsorption $TiO_2$-TiN interfaces as a model of oxidised TiN is our recently published work [54]. In our work [54], we showed that the most favourable structure for adsorbed water on the 4-layer thick (bulk-like) rutile surface on $TiO_2$–TiN is identical to a pure rutile (110) surface. Although the introduction of O several vacancies leads to the formation of highly disordered domains in the interface, the interfacial relaxations do not extend through the bulk and do not affect the geometry of the outermost rutile layers. An adsorbed water monolayer in which the $H_2O$ molecules are aligned on the rutile surface is the most stable configuration on perfect and O-defective 4-layer thick $TiO_2$-TiN interfaces. This is due to the H bonds that are formed between adjacent molecules along the [100] direction. The calculated adsorption energy was found stronger at oxygen defective interfaces due to the higher concentration of reduced $Ti^{3+}$, with an important contribution of interfacial atomic relaxations within the oxide layer.

With limited knowledge of the structural and electronic properties of ultra-thin $TiO_2$ supported on TiN and with the aim to understand how the resulting interface properties can be controlled by the thickness of the deposited oxide, in this paper we present a detailed investigation of $TiO_2$-TiN interfaces with 1 and 2-layer rutile $TiO_2$ (110). We applied Hubbard-Corrected Density Functional Theory (*DFT+U*) simulations to account for potential reduced $Ti^{3+}$ states in the oxide layer. We discuss the structural and electronic properties of ultra-thin $TiO_2$ on TiN,

View Article Online
DOI: 10.1039/C9CP04505B





including the formation of defects in the interfacial region and on the oxide surface. Finally, we present a systematic study of water adsorption and coverage on the ultra-thin $TiO_2$ layer at TiN. Based on ab-initio atomistic thermodynamics analyses, we discuss the thermodynamic stability of water adsorbed at the oxide-nitride system at realistic temperatures and within a range of oxygen and water pressure conditions. The simulations carried out provide a comprehensive insight into the structural and electronic properties of ultra-thin $TiO_x$ supported on TiN, presenting this interfacial system as a promising interface for catalysis. The main outcomes of this study can be used as a guide for the rational design of novel catalysts containing ultra-thin $TiO_2$.

## 2. Computational Details

We carried out periodic Density Functional Theory (DFT) calculations within the framework of the Vienna Ab Initio Simulation Package (VASP). The projector augmented-wave (PAW) potentials [59, 60] are used to describe the core-valence interaction, with the valence electrons described by periodic plane waves with cut-off energy of 400 eV. We used the generalized gradient approximation (GGA) for the exchange-correlation functional as formulated by Perdew and Wang (PW91) [61]. All the calculations in this study include a correction for on-site Coulomb interactions (DFT+U) [62], with U = 4.5 eV applied on the Ti 3d electrons in $TiO_2$. This correction is applied to account for the potential reduction of Ti atoms. It is known that U values larger than 4.20 eV allow the recovery of the experimentally observed gap state in O vacancy rutile (110), compared to standard DFT [63]. In addition, several subsequent works [64-66] used U = 4.5 eV to describe the charge localisation in defective and surface modified $TiO_2$. The chosen U value is also in consistency with our previous works on $TiO_2$-TiN interfaces [40, 54]. We use Bader charge analysis [67] to assess the localization of reduced Ti cations. In a stoichiometric $TiO_2$ slab, all Ti ions ($Ti^{4+}$) have computed Bader charges of *ca.* 1.3 electrons and when $Ti^{3+}$ species are formed, e.g. through oxygen vacancy formation, the computed Bader charges are *ca.* 1.7 electrons, which signifies a $Ti^{3+}$. In addition, the computed spin magnetisations are 0.0 $\mu_B$ for $Ti^{4+}$ cations and *ca.* 0.95 $\mu_B$ for $Ti^{3+}$ cations.

The U correction was also implemented during the ionic relaxation to evaluate the changes that the reduced Ti centres may induce in the oxide's structure. The convergence criteria used for energy and forces on each atom and $10^{-4}$ eV and 0.02 eV/Å respectively.

We calculated the equilibrium lattice for the bulk TiN (a = 4.26 Å) and rutile $TiO_2$ (a = 4.64 Å; c = 2.97 Å) using a Monkhorst-Pack sampling grid of (14 x 14 x 14) k-points and (4 x 4 x 4) k-points respectively. Rutile $TiO_2$ (110) and TiN (100) surfaces have the lowest surface energy for their respective polymorphs and compositions [68, 69]. Upon cleaving from the bulk, the 5-layer thick (10.66 Å) rock-salt TiN (100) surface is composed of neutral planes, each with TiN stoichiometry. The 1-layer and 2-layer thick O–Ti–O tri-layer $TiO_2$ slabs have an approximate thickness of 2.78 Å and 5.55 Å respectively, and exhibit rutile (110) surface structure before relaxation. A vacuum thickness about 18 Å was introduced between the interface slabs to avoid interactions along the normal between the opposite sides of the model interface. The TiN (100) supercell surface model has 120 atoms and lattice parameters of $a$ = 8.51 Å; $b$ = 12.77 Å. The stoichiometric rutile $TiO_2$ (110) 1-layer and 2-layer thick surfaces contain 36 and 72 atoms respectively, with equilibrium lattice dimensions of $a$ = 8.92 Å; $b$ = 13.12 Å. We applied a strain (compression) to $TiO_2$ of 2.7% along [$1\bar{1}0$] and 4.6% in the [001] direction to match the TiN lattice constant, which is a reasonable limit compared to experimental measurements on the rutile $TiO_2$ (110) growth on (100)-oriented TiN, in which a lattice mismatch of up to 8.69% is possible [39]. We use a (2x1x1) Monkhorst-Pack sampling grid during ionic relaxation. After convergence is achieved, we run single point calculation with a (6x4x1) grid to obtain more accurate Partial Density of States (PDOS) for the pristine interfaces. Methfessel-Paxton smearing function with σ = 0.1 eV was employed to integrate the Brillouin Zone. Relevant structure files together with the main output files from our DFT calculations are available via the Nomad repository (*DOI to be added at proof stage*).

The interfacial binding energy is estimated from the difference in energy between the TiN (100) surface slab, the corresponding $TiO_2$ slab (at the lattice constant used in the interface model) and the total energy of the relaxed $TiO_2$-TiN interface. The total energy of the individual TiN and $TiO_2$ slabs were calculated with the same lattice parameters and computational setup as for the interfaces. The contribution to the total energy from the strain of $TiO_2$ was not taken into account in our approach, which aims to provide an estimate of the strength of the interfacial interaction. In addition to the perfect $TiO_2$-TiN stoichiometric system, we also considered the formation of off-stoichiometric systems arising from the formation of O and Ti vacancies. The vacancy formation energy for $n$ simultaneously introduced O vacancies, and normalized by the number of vacancies, is given by the following expression

$$E(O)_{vac} = (E_{defective} - E_{stoichiometric} - n \cdot E_{O_2}/2)/n \quad (1)$$

Where $E(O)_{vac}$ is the vacancy formation energy, $E_{defective}$ is the total energy of the relaxed system after the vacancy formation, $E_{stoichiometric}$ is the total energy of the initially non-defective interface, $n$ is the number of vacancies introduced in the system and the $E_{O_2}/2$ term corresponds to one half of the total energy of an isolated $O_2$ molecule.

On the other hand, if the O vacancies are progressively introduced, the formation energy for the first vacancy is given by:

$$E(O^1)_{vac} = E^1_{defective} - E_{stoichiometric} - E_{O_2}/2 \quad (2)$$

Where $E(O^1)_{vac}$ is the formation energy for the first vacancy and $E^1_{defective}$ is the total energy of the relaxed defective system. Analogously, the formation of the *n-th* vacancy (for n ⩾ 2) is computed from:

$$E(O^n)_{vac} = E^n_{defective} - E^{n-1}_{defective} - E_{O_2}/2 \quad (3)$$

View Article Online
DOI: 10.1039/C9CP04506F



Where $E^{n-1}_{defective}$ is the total energy of the system containing n-1 O vacancies.

The Ti vacancy formation energy is calculated by an analogous expression, in which $E_{O_2}/2$ is substituted by the energy of a single Ti atom within a bulk hexagonal close-packed (hcp) lattice. The energy of an isolated $O_2$ molecule was calculated using a Γ-point sampling grid, an orthogonal supercell with sides larger than 15 Å to avoid molecule self-interaction and the same plane wave cut-off and convergence criteria as the slabs.

The adsorption of water was simulated by the deposition and further relaxation of $H_2O$ molecules at low coordinated Ti sites on the $TiO_2$ surface. Water dissociation (hydroxyl) was created by binding one hydrogen atom from water near the closest low coordinated surface O site. The adsorption energies ($E_{ads}$) per adsorbed water were computed for molecular and dissociative adsorption modes using the following expression:

$$E_{ads} = (E_{hydrated} - E_{surf} - n \cdot E_{H_2O})/n \quad (4)$$

Where $E_{surf}$ and $E_{hydrated}$ are the total energy of the system before and after the adsorption of water respectively. The energy of a single water molecule is multiplied by the number of waters in the system (*n*). As for molecular oxygen, the energy of an $H_2O$ molecule was calculated using the same supercell, Γ-point sampling grid and 400eV plane wave cut-off.

To analyze the relative thermodynamic stability of the interface models in a realistic environment, we use the DFT-derived total energies as input into an atomistic thermodynamic framework. Here, we assume that the interfaces are in equilibrium with two infinite gas reservoirs (i.e. $O_2$ and $H_2O$) that can exchange particles with no change in their chemical potential. This allows us to include in the effect of the surrounding gas phase in thermodynamic equilibrium with the surface. The interface energy can then be calculated as follows:

$$\gamma(p,T) = 1/A[G - \sum N_i \mu_i(p,T)] \quad (5)$$

where *A* is the interface area; *G* is the Gibbs free energy of the crystal; $\mu(p, T)$ is the chemical potential of the atomic species in *i* the system; and the term $N_i$ is the total number of atoms of species *i*. We assume that $O_2$ and $H_2O$ reservoirs are in non-equilibrium with each other. Therefore, we can plot the interface energy as a function of the species of interest by treating the chemical potentials as independent variables, so that a broad spectrum of environmental conditions can be treated. Furthermore, by approximating water vapour and oxygen as ideal gases, we explicitly introduce pressure and temperature in our model through the analytic relation between chemical potentials and the temperature and pressure of the two gas reservoirs as follows:

$$\mu_O(p,T) = \left[\frac{1}{2}E_{O_2} + \mu'_{O_2} + k_B T ln\left(\frac{p_{O_2}}{p^0}\right)\right] \quad (6)$$

$$\mu_{H_2O}(p,T) = \left[E_{H_2O} + \mu'_{H_2O} + k_B T ln\left(\frac{p_{H_2O}}{p^0}\right)\right] \quad (7)$$

Here, *T* and *p* represent the temperature and partial pressure of the two gases, $p^0$ denotes atmospheric pressure and $k_B$ is the Boltzmann constant. $\mu'$ is the energetic term that includes contributions from rotations and vibrations of the molecule, as well as the ideal-gas entropy at 1 atm which can be calculated or taken from experimental values listed in thermodynamic tables [70]. A more detailed description of the methodology can be found in our previous works [54, 71, 72].

## 3. Results and Discussion

### 3.1 Structure of ultra-thin $TiO_2$ on TiN substrate

The DFT optimized lattice constants for the bulk cubic rock-salt structure TiN (*a* = 4.26 Å) and the tetragonal rutile $TiO_2$ (*a* = *b* = 4.64 Å and *c* = 2.97 Å) are used to generate the $TiO_2$ (110) and TiN (100) surface models. Rutile $TiO_2$ (110) and TiN (100) are the most stable low-index crystal cuts for rutile $TiO_2$ [41] and TiN [73]. The rutile $TiO_2$ (110) structure exhibits two types of oxygens on the surface: the two-fold coordinated oxygen ($O_{2f}$), that bridge two Ti atoms on the surface, and the three-fold coordinated oxygens ($O_{3f}$). There are also two types of surface Ti: the five-fold coordinated ($Ti_{5f}$) and the six-fold coordinated ($Ti_{6f}$) which is bridged by two bridging $O_{2f}$ and these alternate along the [001] direction.

To minimize the lattice mismatch between both surfaces, a rutile (110) (3x2) surface supercell, with equilibrium lattice constants *a* = 8.91 Å; *b* = 13.12 Å was generated and compressed in-plane to match the TiN (100) (2x3) surface supercell with lattice parameters of *a* = 8.51 Å; *b* = 12.77 Å, which minimises the lattice strain in $TiO_2$. In our approach, the oxide grows on the TiN and thus it has to accommodate to the substrate structure. The free-standing 2-layer $TiO_2$ preserves the rutile symmetry after DFT relaxation, both at the equilibrium and compressed lattice. On the other hand, the 1-layer model is strongly disordered, as can be observed in Figure R1. While the instability of an isolated $TiO_2$ monolayer could be expected, we are using this as a reference for the stability of a 1-layer oxide interfaced with TiN which would be formed by oxidation of the TiN. Details of this 1-layer model are presented in Figure S1 of the supporting information.

The interface with 1-layer thick $TiO_2$ was generated by removing the outermost O-Ti-O tri-layer from the 2-layer thick model. This approach was chosen to start with better initial nitride-oxide interfacial bond distances, and thus, reduce the appearance of artefacts that may lead to excessive deformation of the $TiO_2$ monolayer. By minimizing the distortions due to lattice mismatch, we can also expect to obtain a more stable $TiO_2$ monolayer. More details on the construction of the interfaces and the structural and electronic properties of $TiO_2$ (110)–TiN (100) interfaces can be found in a previous publication [54].

Figure 1 shows the structure of the 1-layer and 2-layer thick $TiO_2$ (110)–TiN (100) interfaces. Surface Ti atoms on the TiN slab migrate from their initial positions on the surface to bind with oxygen, leading to the formation of multiple Ti-O interfacial

bonds that will promote interface stability [54]. We do not observe structural changes in the subsurface TiN layers.

The overall stability of the $TiO_2$ layers increases when deposited on TiN. The calculated interfacial binding energies for the deposition of the compressed $TiO_2$ slab on TiN are -3.22 eV, which correspond to 0.40 eV per Ti-O interfacial bond, for the 1-layer slab; and -1.66 eV, corresponding to 0.33 eV per bond, for the 2-layer slab.

The formation of reduced $Ti^{3+}$ cations in the oxide is assessed by computing Bader charges. The charge transfer to $TiO_2$ forms reduced $Ti^{3+}$ cations that are indicated by light green atoms in Figure 1. In the 1-layer model, we find computed Bader charges of between 1.32-1.35 electrons for $Ti^{4+}$ sites and between 1.72-1.80 electrons for the $Ti^{3+}$ atoms in $TiO_2$. In the 2-layer structure, the computed Bader charges range between 1.28-1.33 electrons for $Ti^{4+}$ sites and 1.67-1.77 electrons for the reduced $Ti^{3+}$ sites. The spin magnetizations of $Ti^{3+}$ centres in both models have absolute values of 0.9 $\mu_B$. The reduction of Ti species in oxide-metal interfaces, where the metal may transfer electrons to the oxide upon interface formation, has been also observed in other metal-oxide interfacial systems such as $TiO_2$-NiTi[74], $TiO_2$-Cu[75], $CeO_2$-Cu[76], $CeO_2$-Pt[77] or $CeO_2$-Ag [78]. The 1-layer thick $TiO_2$ in Figure 1(a) relaxes into a highly distorted structure when interfaced with the TiN surface. Surface Ti atoms in TiN migrate by up to 0.7 Å from their initial position to bind with O atoms upon interface formation. The oxide layer covers the entire TiN surface and, typically for such thin layers, it does not preserve the symmetry present in the rutile (110) structure. From the top view, we observe hexagonal-like patches that resemble a flattered rutile (100) geometry surface and the oxide is clearly distorted. The formation of highly disordered structures has been observed in other ultra-thin $TiO_2$ films supported on metal surfaces including Ag (100) [79] or Ni (100) [80]. In the oxide slab, five out of the six reduced $Ti^{3+}$ are undercoordinated five-fold ($Ti_{5f}$) species and the remaining $Ti^{3+}$ is six-fold ($Ti_{6f}$) coordinated. For the non-reduced $Ti^{4+}$, one half are $Ti_{6f}$ coordinated to neighbouring O and the remaining three titanium bind to up to five oxygen atoms. The reduced $Ti^{3+}$ atoms in the oxide are aligned along the equivalent $[1\bar{1}0]$ direction and localized on the Ti species that would correspond to $Ti_{5f}$ atoms on an undistorted crystalline single layer rutile (110). The high concentration of $Ti^{3+}$ (half of the total Ti atoms in the oxide), with larger atomic radii compared to $Ti^{4+}$, along with the compression applied to $TiO_2$ to compensate the lattice mismatch with TiN may explain the significant distortions and the formation of this non-ordered oxide monolayer.

In the 2-layer thick model (Fig.1(b)) the rutile (110) structure is clearly preserved. The migration of Ti from the nitride towards the oxide is between 0.3 and 0.8 Å upon interface relaxation. The $TiO_2$ octahedra rotate perpendicularly to the [001] axis, due to the strain applied to compensate the lattice mismatch with TiN along with the presence of reduced $Ti^{3+}$ centres, which are preferentially located in the interfacial region. The features observed in the structure of 2-layer thick $TiO_2$ - TiN interfaces are consistent with our previous model with a thicker oxide layer [40].

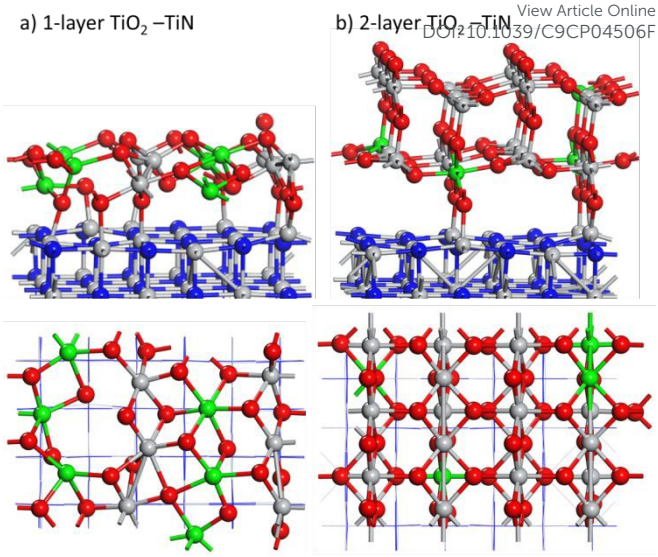


Figure 1. Structure of the stoichiometric rutile $TiO_2$ (110)–TiN (100) interface models. The figures show the front perspective and top view of (a) interface with 1-layer thick $TiO_2$ and (b) interface with 2-layer thick $TiO_2$. Reduced $Ti^{3+}$ atoms in $TiO_2$ represented by green spheres, $Ti^{4+}$ atoms in $TiO_2$ and all Ti in TiN are grey, N atoms are blue and O atoms are red.

### 3.2 Defects in $TiO_2$-TiN interface models

In this section we increase the complexity of the interface models and examine the structural stability of non-stoichiometric structures, starting from perfect one and two-layer $TiO_2$-TiN interfaces. Previous experimental studies have detected that defects can arise during oxide growth and will, therefore, affect the properties of metal-oxide interfaces [39, 81]. We discuss the formation of O vacancies [81] in $TiO_2$, which can be created by thermal annealing and is the most common defect in other metal-oxides. We also evaluate the presence of Ti vacancies in TiN that can form due to surface Ti migration on the TiN surface when this is in contact with atmospheric $O_2$ [37, 39].

Figure 2 shows the structure and energy cost for the formation of the most stable O vacancies in the 1-layer thick oxide model. Figure 2(a) shows the structure of the stoichiometric interface along with the suggested transition pathway towards the formation of the O-defective system. We performed relaxations on different model structures to find the most energetically favourable defect sites. The O vacancy site, indicated in yellow, is the most stable vacancy site among many possible vacancies, and its vacancy formation energy cost is only 0.51 eV with respect to the perfect interface (equation (2)). Upon relaxation of the defective system, one of the oxygen atoms nearest the vacancy (labelled as $O^1$ in Figure 2(a)) migrates to occupy the vacant site above a surface Ti on the TiN surface. The O atoms that are neighbours of $Ti^{1'}$ (namely $O^1$, $O^2$ and $O^3$) go through relaxation following the transition path indicated with red arrows in Figure 2(a). The introduction of an oxygen vacancy does not lead to the formation of extra $Ti^{3+}$ in the oxide, as can be expected from the absence of an $O^{2-}$ anion. In this case, the

View Article Online
DOI: 10.1039/C9CP04506F

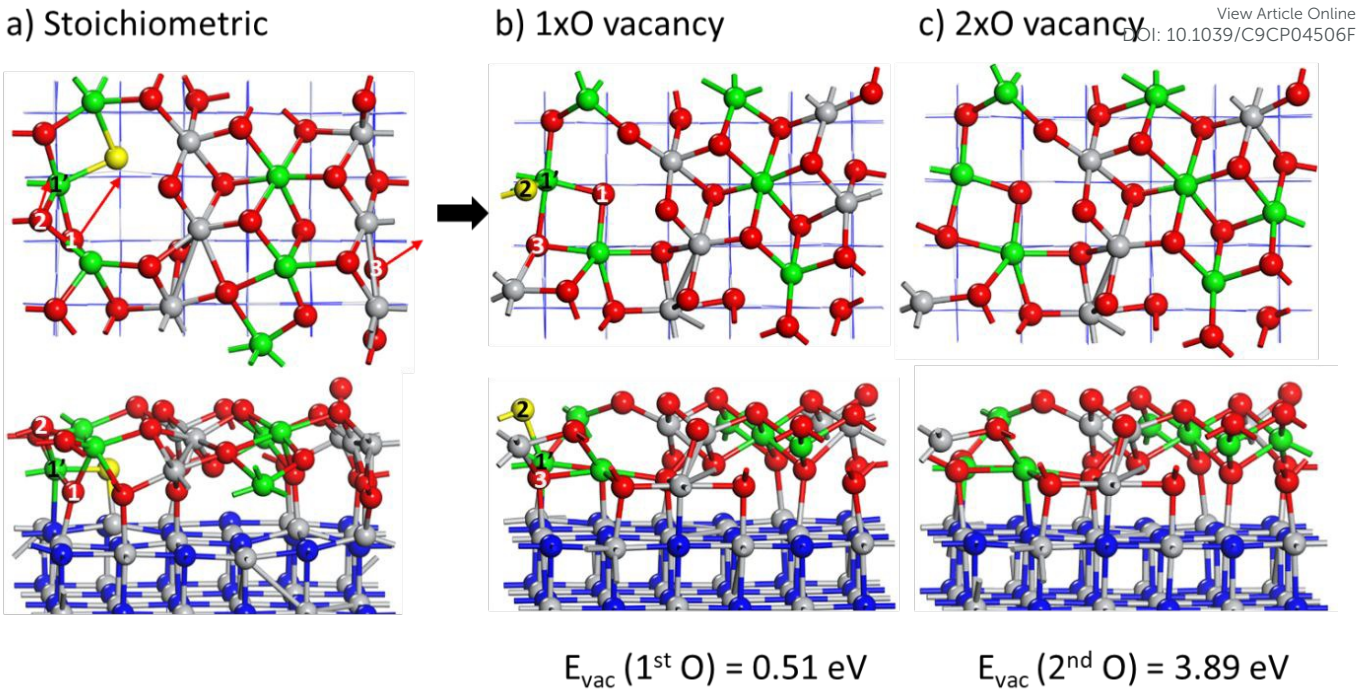


Figure 2. Structure of the O-defective 1-layer thick rutile $TiO_2$ (110)–TiN (100) interface models. We present (a) the initial stoichiometric model with arrows indicating the suggested transition pathway towards the formation of (b) the system with one oxygen vacancy; (c) shows the interface with 2xO vacancies. The figures for the non-stoichiometric systems show the front perspective and top view of the interfaces. The oxygen vacancy sites are represented in yellow, reduced $Ti^{3+}$ atoms in $TiO_2$ are represented by green spheres, $Ti^{4+}$ atoms in $TiO_2$ and all Ti in TiN are grey, N atoms are blue and O atoms are red.

creation of an O vacancy in an already highly reduced oxide slab tends to favour delocalization (with computed Bader charges of 1.41 electrons, which signifies partial reduction) and the extra electrons are therefore evenly distributed around the oxide.

Given the low cost for the formation of the first oxygen vacancy, we also discuss the formation of a second O vacancy (Figure 2(c)). Taking as initial structure the system in which the first vacancy was created (Figure.2(b)), we found $O^2$ to be the most stable O-vacancy site on the oxide's surface. The formation energy for the second O vacancy is significantly increased, with a computed formation energy of 3.89 eV with reference to the single O-vacancy structure (equation (3), with n=2). The addition of two more electrons in an already highly reduced system, in which further relaxation could be hindered, can explain the high energy cost for the second O vacancy. We do not observe a significant distortion in the system produced by this second O vacancy despite the further reduction that arises in the oxide from the vacancy. In addition to the sequential formation of O vacancies, we also considered the simultaneous formation of two vacancies in the stoichiometric $TiO_2$ slab. We chose the most favourable O vacancies from the sequential formation (namely $O^1$ and $O^2$) and removed these from the perfect interface. The relaxed structure is presented in Figure S2. The formation energy, calculated with equation (1), results in a total value of 5.71 eV for the 2 O vacancies (2.86 eV/$O_{vac}$). This is 1.31 eV higher than the accumulated energy from the sequential formation of 2 vacancies, introduced one by one. Thus, we conclude that the simultaneous formation of 2 O vacancies is less favourable than the sequential formation.

The computed Ti vacancy formation energy in TiN interfaced with the 1-layer thick oxide is as high as 4.62 eV, therefore we do not consider this defective interface for further study. The structure of the 1-layer interface with a Ti vacancy is discussed in the supporting information, Figure S3.

Figure 3 shows the relaxed structure of 2-layer $TiO_2$-TiN interfaces with one O vacancy. We differentiate between vacancies created in (a) the terminating surface layer or (b) in the interfacial region. We computed formation energy values of 4.06 eV for an $O_{2f}$ bridging surface oxygen vacancy in the terminating layer and 3.85 eV for an interfacial vacancy bridging $TiO_2$ and TiN. The calculated O vacancy energy values are slightly larger than those in the 4-layer thick rutile (110) -TiN model (3.40 eV at the interface) or a surface O vacancy in perfect rutile (110) surface (3.66 eV) [63], while the energy is more favourable than the formation of O vacancies in bulk rutile ($E_{vac}$ = 4.4 eV) [82]. The two non-stoichiometric structures are stable, and the rutile structure does not show significant distortions after the vacancy formation. Although the difference in energy between these two models is quite small, we should take into account that surface defects may form from initially perfect interface under certain ambient conditions like the exposure to high temperatures while interfacial defects are most likely to arise and remain trapped upon oxidation of TiN.

In our previous study, we found that the introduction of several O vacancies becomes more favourable, leading to the stability of highly non-stoichiometric systems [40]. Based on these results, in addition to the single vacancy system in the 2-layer thick $TiO_2$ model, we also consider the formation of highly non-

stoichiometric interfaces, in which all of the bridging O are removed from the interface region. Figure 4 depicts the structure of 2-layer thick interface models with 6 interfacial oxygen vacancies, which results in an interface with the oxide composition of $TiO_{1.75}$-TiN.

We considered two different approaches to generate this defective interface to explore the effect of different structures. The **etched model** in Figure 4(a) was generated by removing the 2 outermost O-Ti-O tri-layers from a 4-layer thick $TiO_{2-x}$-TiN model that already contained 6 oxygen vacancies ($TiO_{1.88}$-TiN). The initial structure of this interface is available in the Nomad repository [83]. The interface in Figure 4(b) (denoted the slab model) was generated by removing all the interfacial bridging oxygen in the perfect model from Figure 1(b). Both highly defective structures are stabilized by the formation of multiple Ti-O bonds within the interfacial region upon relaxation. In the etched model, the symmetry of rutile (110) structure is preserved on the surface, with a strongly distorted $TiO_2$ layer in the interfacial region, where some atoms occupy an interstitial-like position within the rutile structure. The slab model forms a highly distorted non-ordered oxide structure in which the crystalline patterns of the rutile structure are hardly identifiable. The total energy of the model with non-ordered $TiO_{2-x}$ more stable than the etched oxide structure by 7.8 eV. This higher stability originates from multiple interfacial Ti-O bonds formed in the slab model upon DFT relaxation, compared to the etched interface, and indicates that distorted $TiO_2$ layers are more stable.

We identify 14 reduced $Ti^{3+}$ cations in the non-ordered oxide compared to 11 $Ti^{3+}$ sites in the etched model. The formation of extra reduced cations is expected after the introduction of many O vacancies and certainly influences the distortions in the rutile structure.

The formation energy of the O vacancies simultaneous created in the stoichiometric $TiO_2$-TiN model, to form the $TiO_{1.75}$-TiN system, is 3.15 eV / $O_{vac}$ in the **etched** structure and 1.85 eV / $O_{vac}$ in the **slab model**, as calculated from equation (1). The introduction of multiple vacancies in an already non-stoichiometric system has a lower energy cost compared to the formation of the first O vacancy at the stoichiometric system ($E_{vac} \geq 3.85$ eV). The suggested stability of the highly non-stoichiometric interfaces is consistent with our previous study, although our energy values are higher than the formation of the non-stoichiometric $TiO_{1.82}$-TiN system in an interface with 4-layer thick oxide (1.30 eV / $O_{vac}$) [40].

Despite the large difference in energy between the etched and slab models, both crystalline and disordered $TiO_2$ models can be stabilized and even coexist depending on the growth temperatures and techniques. In particular, it has been shown in a previous ab-initio molecular dynamics work that at high temperatures, an ordered oxide structure can grow on the TiN surface, while at low temperatures vacancies and defects are prone to remain trapped inside the oxide structure [37]. We should note that although our approach considers the formation of vacancies from a perfect interface, the most likely origin of defect formation is during oxide growth and these defects can be trapped in the interface after the $TiO_x$ growth of TiN and subsequently affect the structure and electronic features of the interfacial system.

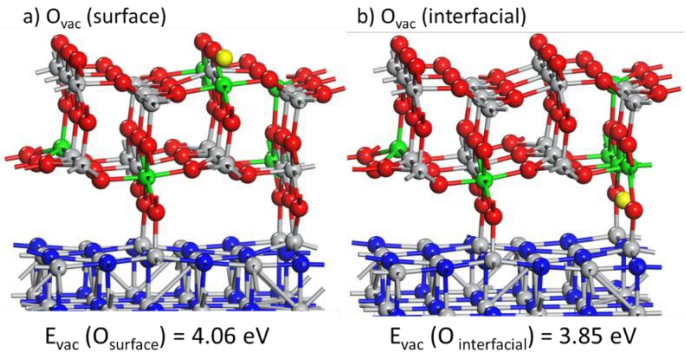


Figure 3. Structure of the O-defective 2-layer thick rutile $TiO_2$ (110)–TiN (100) interface models with (a) one surface O vacancy and (b) interfacial O vacancy. Figures on the top panel represent the frontal perspective view, the top view is shown on the bottom panel and the vacancy formation energy calculated taking as reference molecular $O_2$ is given below the figures. In the figure, the oxygen vacancy sites are represented by yellow spheres, reduced $Ti^{3+}$ atoms in $TiO_2$ are represented are green, $Ti^{4+}$ atoms in $TiO_2$ and all Ti in TiN are grey, N atoms are blue and O atoms are red.

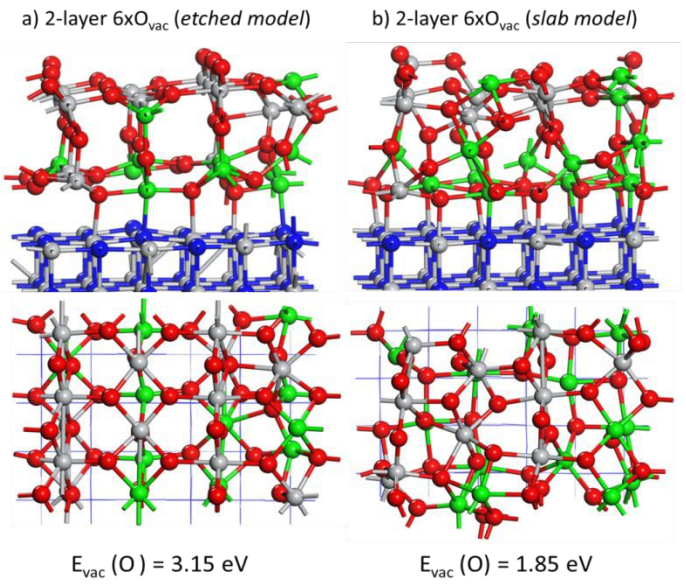


Figure 4. Structure of the 2-layer thick rutile $TiO_2$ (110)–TiN (100) interface models with 6 oxygen vacancies in the interface. The two different models are created by (a) removing 2 O-Ti-O tri-layers from the 4-layer thick models from reference40, etched model, and (b) introducing 6 interfacial O vacancies in the 2-layer thick model in Figure 1.b, slab model. Figures on the top panel represent the frontal perspective view, the top view is shown on the bottom panel and the vacancy formation energy calculated taking as reference molecular $O_2$ is given below the figures. In the figure, the oxygen vacancy sites are represented by yellow spheres, reduced $Ti^{3+}$ atoms in $TiO_2$ are represented are green, $Ti^{4+}$ atoms in $TiO_2$ and all Ti in TiN are grey, N atoms are blue and O atoms are red.

### 3.3 Water adsorption at ultra-thin $TiO_2$ models on TiN

#### 3.3.1 Adsorption of one water molecule

Water is present in nearly every environment and can interact with metal oxide surfaces such as $TiO_2$. Therefore, it is

View Article Online
DOI: 10.1039/C9CP04506F





important to understand how the presence of water can alter fundamental properties of $TiO_2$ films. In the present section, we discuss the adsorption of water on the previously described oxide-nitride interfaces, including stoichiometric $TiO_2$ and several O-defective $TiO_{2-x}$ models supported on TiN.

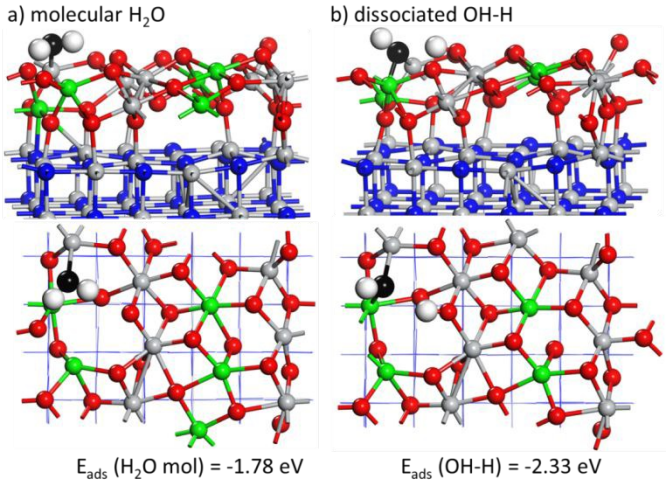


Figure 5. Structure of isolated (a) molecular water ($H_2O$) and (b) dissociated water (OH-H) adsorbed at stoichiometric 1-layer thick $TiO_2$ -TiN interface. The adsorption energy values are presented under figures. The $Ti^{3+}$ atoms in $TiO_2$ are represented by green spheres, $Ti^{4+}$ atoms in $TiO_2$ and all Ti in TiN are grey, N atoms are blue, O atoms from $TiO_2$ are red, O atoms from adsorbed water are black and H atoms are white.

In the interfaces where the usual rutile (110) surface termination is clearly present, such as the stoichiometric 2-layer $TiO_2$-TiN interface, the water molecules are adsorbed on top of a surface $Ti_{5f}$ site, which is the most favourable adsorption site on rutile (110) surfaces [41]. For the interfaces with highly distorted surface terminations, the water molecules were systematically deposited at different under-coordinated Ti atoms exposed on the surface, searching for the most stable adsorption site. For the dissociative adsorption of water, a hydroxyl (OH) from water is kept on the same site as molecular $H_2O$ was adsorbed and the second hydrogen is adsorbed at an adjacent $O_{2f}$ site [41]. We also discuss the stability of molecular water against dissociated, hydroxyl adsorption modes for an isolated $H_2O$ which is equivalent to 1/6 monolayer (ML) coverage, and for fully-covered surfaces (1 ML coverage) on $TiO_2$–TiN interface models.

The computed adsorption energy per water molecule, for molecular and dissociated water adsorption at the different $TiO_2$-TiN interfaces as a function of the water surface coverage, are presented under the relaxed structure figures and summarized in Table S1. The distances for the bonds formed between the rutile surface and the adsorbed species are listed in the supporting information section (Table S2).

The most stable configuration for one isolated water adsorbed on stoichiometric 1-layer thick $TiO_2$-TiN interface is shown in Figure 5. The negative energy indicates that molecular adsorption is favourable, with $E_{ads}$ = -1.78 eV. The dissociation of water contributes to the further stabilization of the model by 0.55 eV, with $E_{ads}$ = -2.30 eV. The bond formed between the adsorbed O and the surface Ti is 2.23 Å for water and 2.05 Å for the hydroxyl.

The adsorption of isolated water on the O-defective 1-layer $TiO_2$–TiN interface (Fig.S2), where $H_2O$ is adsorbed with its O sitting at the vacancy site, behaves similarly to the stoichiometric model. Our results show the preferred dissociation of isolated water on the defective $TiO_2$ layer, with computed adsorption energies of -1.17 eV for molecular and -1.73 eV for dissociated water. The stronger adsorption energy for dissociated water at the stoichiometric $TiO_2$ layer is different from the preference for dissociative water adsorption on defective rutile (110) [53, 84], however our interface model exhibit a distorted geometry in which the surface layer is also different from that of pure rutile (110) and has a larger number of reduced $Ti^{3+}$ species.

On the 2-layer thick stoichiometric $TiO_2$-TiN interface (figure 6), the preference for an isolated water is dissociative adsorption ($E_{ads}$ (OH-H) = -1.09 eV) and this is 0.41 eV more stable than the adsorption of molecular $H_2O$. The adsorption of dissociated water produces a strong distortion on the rutile layer where the Ti migrates outwards by ca. 1.6 Å with respect to its initial position on the bare layer and binds with the OH group.

Adsorption of isolated molecular water at the defective 2-layer $TiO_{1.75}$-TiN interfacial systems (with all interface oxygen removed), using equation (4) from the methodology section results in endothermic adsorption of 1.24 eV on the etched model and 1.54 eV on the slab oxide interface model. The adsorption energy is usually employed as a quantitative description of the new bonds created between the surface and the adsorbates. However, in our case, the total adsorption energy of water is also influenced by a contribution from the atomic relaxations in the $TiO_2$-TiN interface after water is adsorbed, as previously described in Ref[54]. The reference for the energy calculation is the total energy of the initially bare interface model. To estimate the influence that the distortions on the rutile-TiN interface have on $E_{ads}$, we define the distortion energy ($E_{dist}$) as the difference in energy between the pristine interface model (before molecular adsorption) and the relaxed structure after water desorption. If the corresponding $E_{dist}$ is subtracted to the adsorption energy computed taking the pristine surface as a reference; we can get an estimation of the energy of the bonds formed between water and the oxide interface. Both $TiO_{1.75}$-TiN interfaces with isolated $H_2O$ exhibit adsorption energies that are strongly influenced by the interfacial atomic relaxations, which are responsible for an increase in the total energy by 2.33 eV on the etched model and 2.52 eV in the slab oxide model. These values give insights into the strong distortions produced on the oxide layer after water adsorption, which is clear in Figures 7 and 8. On the etched model (Figure 7), dissociative adsorption of $H_2O$, with an adsorption energy of -1.73 eV, is more stable than the molecular mode, for which the adsorption energy is -0.79 eV; these are the adsorption energies using the model of the interface described in the previous paragraph as a reference. The adsorption of water on the etched $TiO_{1.75}$-TiN interface induces a migration along the normal of the Ti that binds with the adsorbed O of 0.48 Å for the molecular adsorption mode, 1.02 Å for the

dissociated model and 0.17 Å after desorption, estimated with respect to the initial position of Ti on the pristine surface. The distances of the Ti-O bonds formed on the surface are 2.11 Å for $H_2O$ and 1.91 Å for OH.

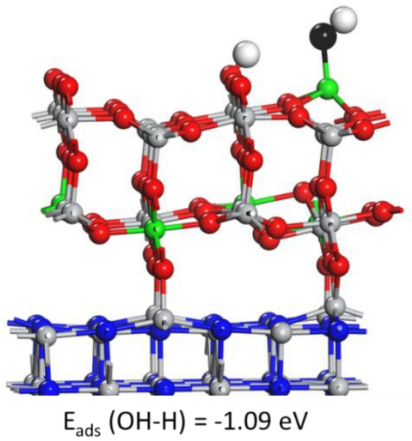


Figure 6. Structures of a single (OH-H) on perfect 2-layer thick rutile (110) $TiO_2$ -TiN interface. The adsorption energy is presented under the figure. The $Ti^{3+}$ atoms in $TiO_2$ are represented by green spheres, $Ti^{4+}$ atoms in $TiO_2$ and all Ti in TiN are grey, N atoms are blue, O atoms from $TiO_2$ are red, the O atoms from adsorbed water is black and H atoms are white.

On the $TiO_{1.75}$-TiN interface generated from the 2-layer slab model (Figure 8), $H_2O$ is adsorbed on the surface forming a Ti-O bond with length 2.20 Å which is shortened to 1.89 Å after dissociation. If we use again the distorted surface as reference, that has higher energy than the initially bare surface, the computed adsorption energy for an $H_2O$ molecule is -1.28 eV and it is more stable than the model containing dissociated water ($E_{ads}$ = -0.87 eV). In addition, an extra $Ti^{3+}$ cation is present in the oxide as a result of electronic relocalisation after water adsorption/desorption process. We can thus conclude that, except for the 2-layer thick slab model interface, which exhibits a strongly distorted surface, all the models for the adsorption of isolated water on $TiO_2$-TiN interfaces show that dissociated water is more stable than molecular adsorption. These differences range from 0.41 eV to 0.94 eV. Our findings are in line with previous theoretical studies of water adsorption on rutile (110) or and 4-layer thick $TiO_2$-TiN interfaces, where the preference for dissociative adsorption for single isolated water molecules at rutile (110) was shown. Our computed energy differences are larger than the 0.11 eV estimated for water dissociation on rutile (110) [55] or 0.34 eV on 4-layer thick $TiO_2$-TiN interface [54]. The present results also show that the adsorption energy of an isolated OH-H is stronger at the 1-layer thick stoichiometric $TiO_2$-TiN interface compared to the thicker oxides or non-stoichiometric models. This is a consequence of the large concentration of reduced $Ti^{3+}$ that arise on surface sites when a very thin $TiO_2$ forms an interface with TiN in combination with the non-ordered structure that contributes towards the further stabilization of this ultra-thin oxide layer.

### 3.3.2 Adsorption of water at higher coverages

At the highest water coverage, the fully covered 1-layer model (Figure 9) has six $H_2O$ molecules deposited on the available Ti under-coordinated sites on the surface. The relaxed structures for the models with molecular and dissociated water are presented in Figure 9(a) and Figure 9(b) respectively. Both models are almost degenerate in energy, with computed adsorption energies per water molecule of -0.81 eV for molecular $H_2O$ and -0.84 eV for OH-H. Closer inspection shows that upon relaxation, 3 water molecules form when starting from the initially fully hydroxylated surface (these are indicated with dashed rings in Figure 9(b)) leading to a mixed environment in which molecular $H_2O$ and hydroxyls coexist. On the molecular $H_2O$ covered surface, five of the $H_2O$ bind to surface Ti with bond distances between 2.22-2.33 Å while one of the molecules interacts with surface O on the surface through a hydrogen bond with an O---H distance of 2.06 Å.

The bonds created between surface Ti and O from $H_2O$ are shorter on the hydroxylated surface. The three OH and the closest $H_2O$ to the surface bind with Ti-O distances between 1.97-2.17 Å. The two remaining water molecules sit further from the surface at distances of 2.77 Å and 2.83 Å from the nearest surface Ti and bind to surface O with Hydrogen-bonds that have O---H distances of 1.88 Å and 1.84 Å. The two adjacent $H_2O$ molecules, at a distance of 1.94 Å, also interact through non-bonding O-H interactions. These results indicate that when a very thin oxide layer is deposited on TiN, forming a nearly amorphous or nanostructured oxide, molecular water may coexist along with hydroxyls when water pressures are equal or higher than regular ambient conditions.

View Article Online
DOI: 10.1039/C9CP04506F

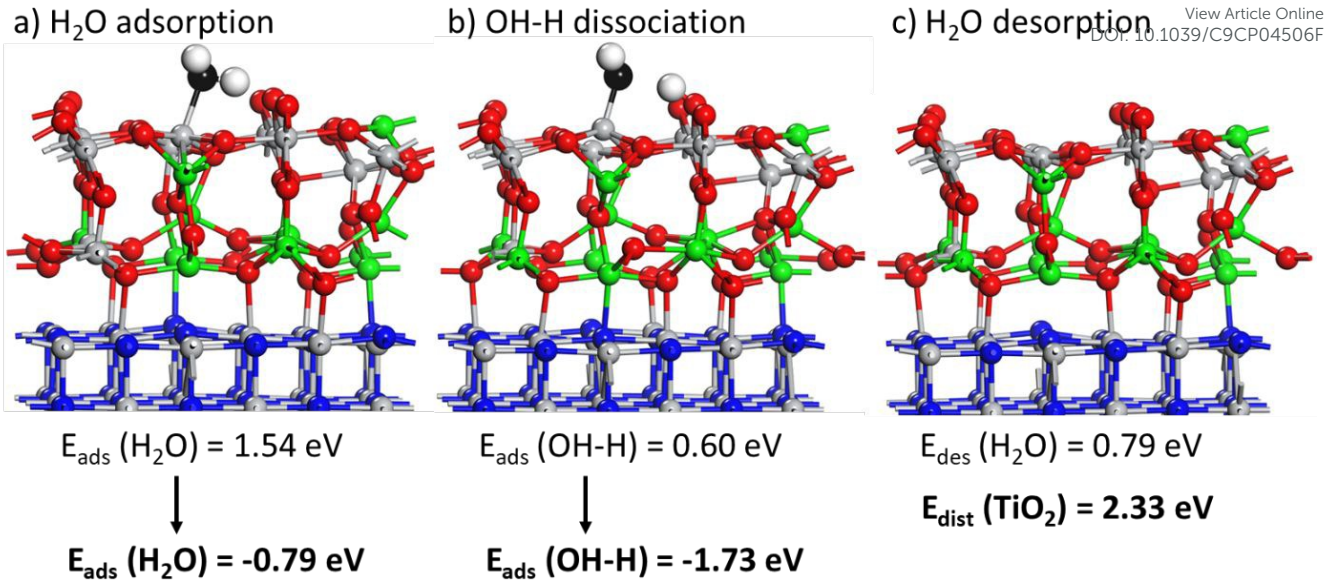


Figure 7. Structure of (a) molecular water ($H_2O$) adsorption, (b) dissociated water (OH-H) adsorption and (c) water desorption at the 2-layer thick etched model of rutile (110) surface on $TiO_2$ -TiN interfaces. The adsorption energy values using the pristine surface as reference (equation 4) is presented directly under (a) and (b) figures. The water desorption energy ($E_{des}$) and the distortion energy ($E_{dist}$), that shows the energy cost for the distortion produced in the original interface and after removing water, are presented under figure (c). The corresponding $E_{ads}$ using the distorted surface (higher energy) as reference are presented in bold and linked with arrows below (a) and (b). The interface structures are represented following the same colour code as the previous figures.

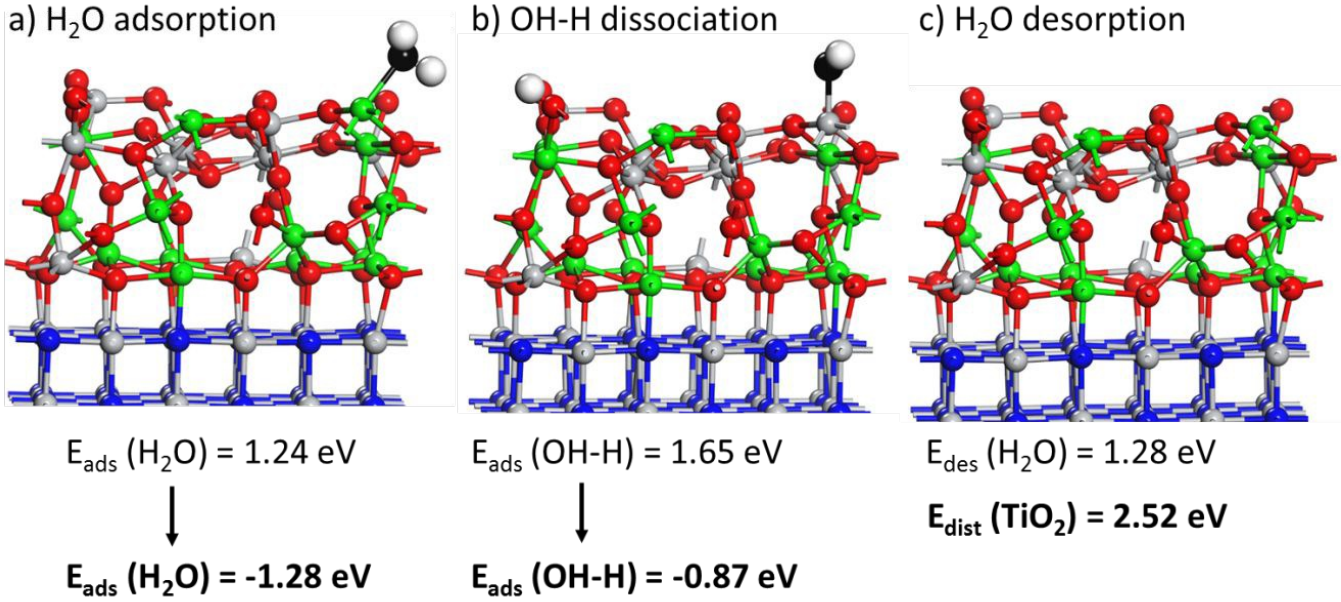


Figure 8. Structure of (a) molecular water ($H_2O$) adsorption, (b) dissociated water (OH-H) adsorption and (c) water desorption at the 2-layer thick slab model of rutile (110) surface on $TiO_2$ -TiN interfaces. The adsorption energy values using the pristine surface as reference (equation 2) is presented directly under (a) and (b) figures. The water desorption energy ($E_{des}$) and the distortion energy ($E_{dist}$), that shows the energy cost for the distortion produced in the original interface and after removing water, are presented under figure (c). The corresponding Eads using the distorted surface (higher energy) as reference are presented in bold and linked with arrows below (a) and (b). The interface structures are represented following the same colour code as the previous figures.

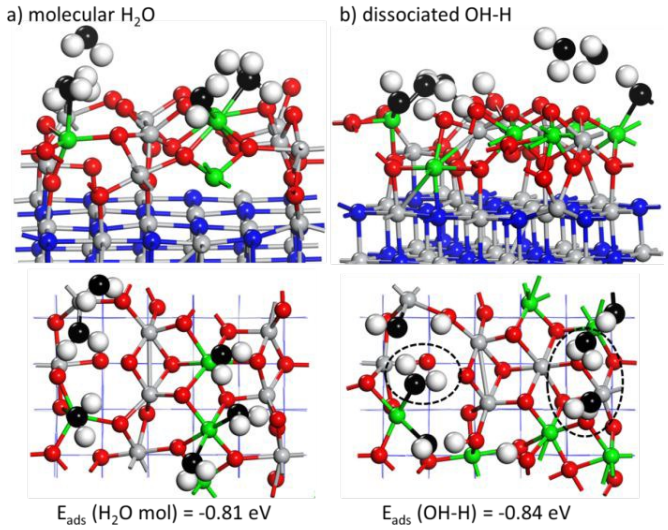


Figure 9. Structure fully covered 1-layer thick $TiO_2$ -TiN interface with (a) molecular water and (b) dissociated water adsorption modes. The adsorption energy values per adsorbed water are presented under figures. Molecular $H_2O$ formed from OH-H reassociation are indicated with dashed rings. The $Ti^{3+}$ atoms in $TiO_2$ are represented by green spheres, $Ti^{4+}$ atoms in $TiO_2$ and all Ti in TiN are grey, N atoms are blue, O atoms from $TiO_2$ are red, O atoms from adsorbed water are black and H atoms are white.

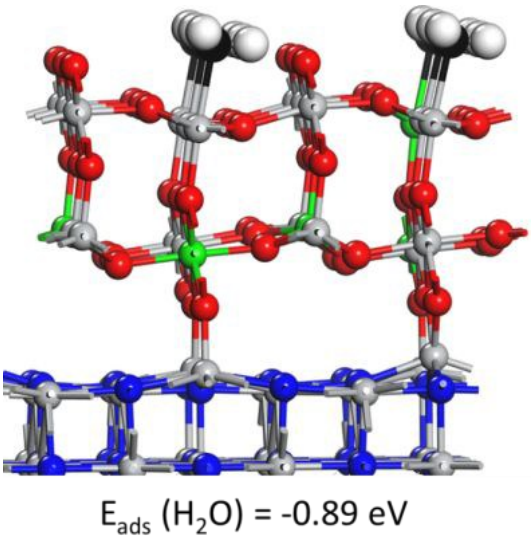


Figure 10. Structure of a water monolayer (1ML) on perfect 2-layer thick rutile (110) $TiO_2$ -TiN interface. The adsorption energy per adsorbed water is presented under the figure. The $Ti^{3+}$ atoms in $TiO_2$ are represented by green spheres, $Ti^{4+}$ atoms in $TiO_2$ and all Ti in TiN are grey, N atoms are blue, O atoms from $TiO_2$ are red, O atoms from adsorbed water are black and H atoms are white.

Moving now to the 2 layer oxide models, molecular water adsorption at full coverage is the most stable on the perfect interface (Figure 10). On the surface, the two rows with 3 $H_2O$ molecules each align on the rutile surface along the $[1\bar{1}0]$ direction via formation of strong H-bonds between adjacent water molecules, stabilizing the fully covered model. The preference for the aligned distribution is in agreement with previous studies on water adsorption at $TiO_2$ rutile (110) [55, 85] and 4-layer thick $TiO_2$-TiN interfaces [54]. On the model with all water molecules dissociated, hydroxyls on the surface go through a barrierless reaction to reassociate and form water molecules (Figure S6), which indicates the instability of dissociated water on fully covered ordered rutile (110) surfaces. The 2-layer thick non-stoichiometric $TiO_{1.75}$-TiN models allow accommodating up to five $H_2O$ binding directly to surface Ti through the formation of Ti-O bonds. The interfacial and surface relaxations upon vacancy formation leads to the presence of $Ti_{5f}$ sites on the surface that are available for water adsorption, instead of the six available sites on the rutile (110) stoichiometric model. Water adsorbs strongly on the etched $TiO_{1.75}$-TiN interface (Figure 11), due to the contribution of surface relaxations to the overall decreasing of the total energy. The molecular adsorption of $E_{ads}$ = -1.73 eV per water is very similar to the energy of the dissociative adsorption mode with $E_{ads}$ = -1.66 eV.

The two models display a mixed $H_2O$ and OH coverage on the surface. From a 1 ML coverage of molecular water, one water molecule adsorbs dissociatively upon relaxation, Figure 11(a). On the surface with 1 ML coverage of water in dissociated mode, one water molecule forms upon relaxation, Figure 11(b). The bonds formed between surface Ti and the adsorbed O are consistently larger for molecular $H_2O$ with measured distances in a range between 2.20-2.27 Å from O in $H_2O$ and 2.12 Å from O in OH. The bond distances on the hydroxylated layer vary between 1.88 - 2.01 Å from OH and 2.22 Å from $H_2O$.

The small difference in energy between models along with the coexistence of $H_2O$ and surface OH suggest the likely stability of mixed layer of hydroxyls along with water molecules at high water coverages on non-stoichiometric and distorted rutile (110) interfaces, where the formation of stable $H_2O$ islands may take place.

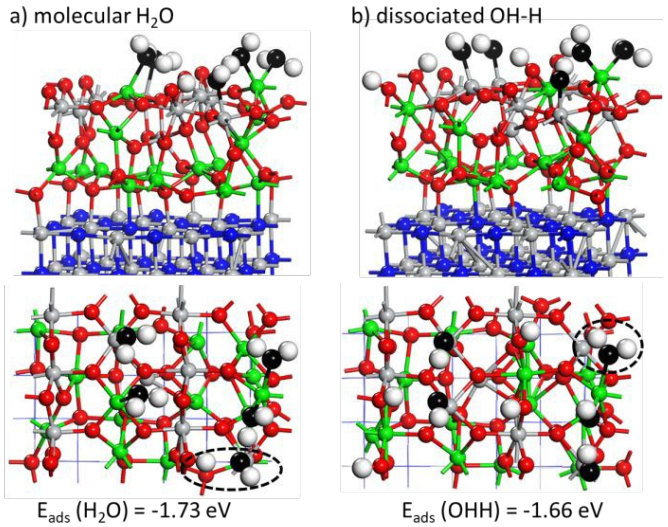


Figure 11. Structures of fully covered 2-layer thick etched model of $TiO_2$ -TiN interfaces with (a) molecular water and (b) dissociated adsorption modes. The adsorption energy values per adsorbed water are presented under figures. The $Ti^{3+}$ atoms in $TiO_2$ are represented by green spheres, $Ti^{4+}$ atoms in $TiO_2$ and all Ti in TiN are grey, N atoms are blue, O atoms from $TiO_2$ are red, O atoms from adsorbed water are black and H atoms are white.

View Article Online
DOI: 10.1039/C9CP04505E



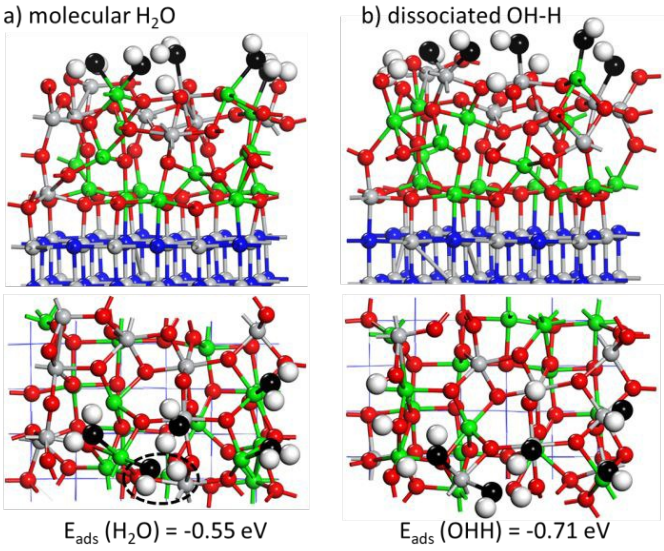


Figure 12. Structures of fully covered 2-layer thick slab model of $TiO_2$ -TiN interfaces with (a) molecular water and (b) dissociated adsorption modes. The adsorption energy values per adsorbed water are presented under figures. Molecular $H_2O$ that dissociates spontaneously to form OH-H is indicated with a dashed ring. The $Ti^{3+}$ atoms in $TiO_2$ are represented by green spheres, $Ti^{4+}$ atoms in $TiO_2$ and all Ti in TiN are grey, N atoms are blue, O atoms from $TiO_2$ are red, O atoms from adsorbed water are black and H atoms are white.

The adsorption of water on the 2-layer thick non-ordered **slab model** $TiO_2$-TiN interface, depicted in Figure 12, leads to a more moderated decrease of the total energy compared to the etched interface, as a consequence of the higher stability of this interface. The fully covered hydroxylated surface ($E_{ads}$ = -0.71 eV per water molecule) is more stable than the $H_2O$ covered model ($E_{ads}$ = -0.55 eV per water molecule). In the latter, one of the $H_2O$ molecules spontaneously dissociates upon relaxation to form an OH-H pair on the surface. The bonds formed between surface Ti and the adsorbed O are again larger for molecular $H_2O$. The Ti-O distances on the molecular model (Figure 12(a)) range between 2.20 - 2.27 Å as measured from O in $H_2O$ and 2.12 Å from O in the single OH on the surface. Bond distances on the hydroxylated layer (Figure 12(b)) range between 1.85 - 1.97 Å as measured from the adsorbed O in the OH termination. The energy difference of 0.16 eV per water with the barrierless dissociation of water on the $H_2O$ covered surface suggest the preferential stability of hydroxyls against molecular water on a highly non-stoichiometric oxide that presents a disordered structure and with a large concentration of reduced $Ti^{3+}$ cations. The preferential formation of hydroxyls as a result of the high concentration of reduced $Ti^{3+}$ in $TiO_2$ induced by UV illumination has been experimentally observed and it is also proposed to increase the hydrophilicity of the surface [18]. Our models show the formation of stable hydroxyls on highly non-stoichiometric $TiO_{2-x}$ surfaces, which contain larger proportions of $Ti^{3+}$ cations than the stoichiometric interfaces and lacks the high order of a crystalline surface layer that permits molecular $H_2O$ to form stable rows or islands on the oxide surface. The computed adsorption energies for water at the 1-layer and 2-layer $TiO_2$-TiN are weaker on the O-defective systems, compared to the stoichiometric oxide slab. However, considering the strongly disordered structure of the oxide slab in these models, the concentration of reduced Ti cations, in an already highly reduced surface, should not be a critical factor for the stability of adsorbed water on the surface, which is primarily affected by the surface morphology in these specific cases.

### 3.4. Thermodynamics of water adsorption at $TiO_2$-TiN

In this section, we analyze the relative stability of the interfaces when they are in thermodynamic equilibrium with the environment. We use the results at 0K obtained by DFT calculations and include the effect of oxygen and water present in the atmosphere. We model the system as it exchanges particles with an external reservoir, which is imagined to be infinitely large so that the chemical potentials of the species do not change during the process.

In the previous section, we calculated the oxygen vacancy formation energies for single and double $TiO_2$ layer on TiN, and we deduced that the formation of a single vacancy is favourable compared to the multiple vacancies in the 1-layer slab while in the 2-layer model the opposite trend is observed. These results are in line with our *ab-initio* thermodynamics analysis, which shows that the inclusion of realistic environmental variable indicates that multiple vacancies are most stable at low (reducing) oxygen chemical potential values.

As shown in Fig.13, in the interface formed by a single $TiO_2$ layer, the single vacancy is the most stable for a very large range of $\Delta\mu_0$, and the highly reduced interface becomes stable only if $\Delta\mu_0$ is lower than -3.0 eV. On the other hand, when a double layer of $TiO_2$ is deposited on TiN, we have two possible distinct scenarios for the formation of a single O vacancy: at the $TiO_2$ surface or at the $TiO_2$-TiN interface. In both cases, the pristine interface is stable at low $\Delta\mu_0$, whereas decreasing $\Delta\mu_0$ the multiple interfacial vacancy system becomes stable. However, the ideal interface shows temperature/pressure “resistance” to reduction if compared to the non-stoichiometric oxide slabs.

When taking into account the effect of the water, we have to include in the model an additional reservoir that is in equilibrium with the interface. However, in our model, the two reservoirs are in non-equilibrium with each other, so that we are able to treat the two variable $\mu_0$ and $\mu_{H2O}$ independently and consequently explore a wider range of possible conditions. In Fig.14 we show the chemical potential of water from 0 to -3.0 eV, however, to consider water vapour as a thermodynamically stable phase, the maximum value that $\Delta\mu_{H2O}$ can assume is −0.91 eV, which corresponds to the chemical potential of water at the experimental critical point.

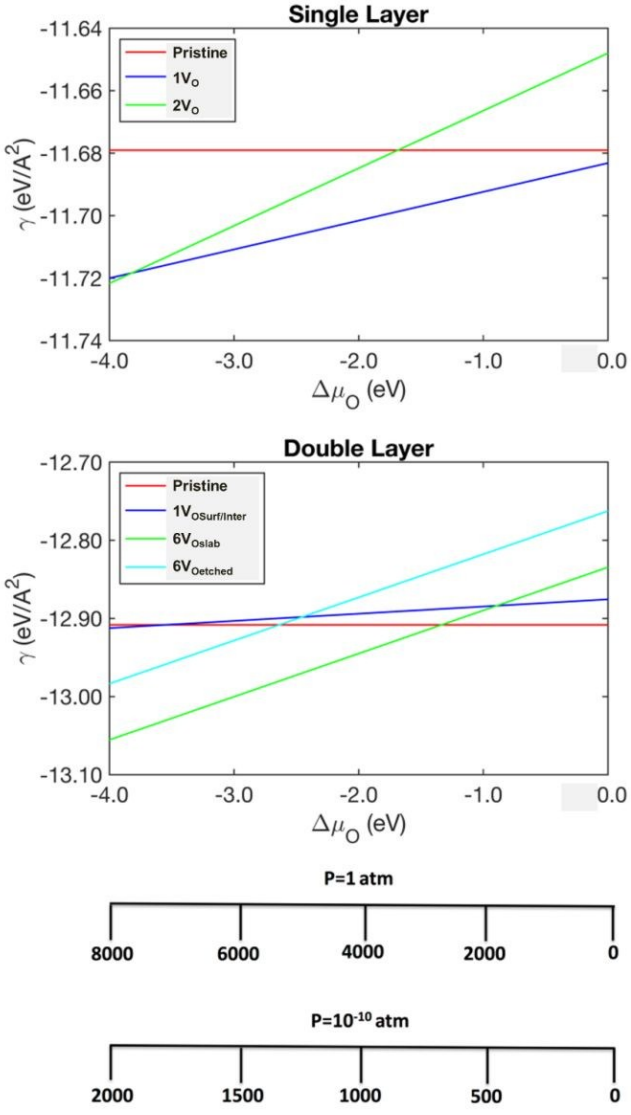


Figure 13. Interface energy (γ) as a function of the chemical potential of oxygen ($\Delta\mu_O$) as defined in the methodology section. Top and bottom plots represent respectively the interface formed by TiN and a $TiO_2$ single and double layer. The negative values of $\Delta\mu_O$ correspond to reducing atmospheric conditions. The red and blue lines represent the interface energy of pristine model and with one oxygen vacancy in the single layer ($1V_O$) and double layer ($1V_{OSurf/Inter}$) models, where the systems with surface and interfacial O vacancy are represented together. The green and cyan represent the interface in highly reduced conditions, that is with two oxygen vacancies for $TiO_2$ single layer ($2V_O$), and six oxygen vacancies for $TiO_2$ double layer in the slab ($6V_{Oslab}$) and etched ($6V_{Oslab}$) models. We include two additional scales that represent the conversion in temperature (K) of the chemical potential of the oxygen, calculated to p=1atm and p=10-10atm

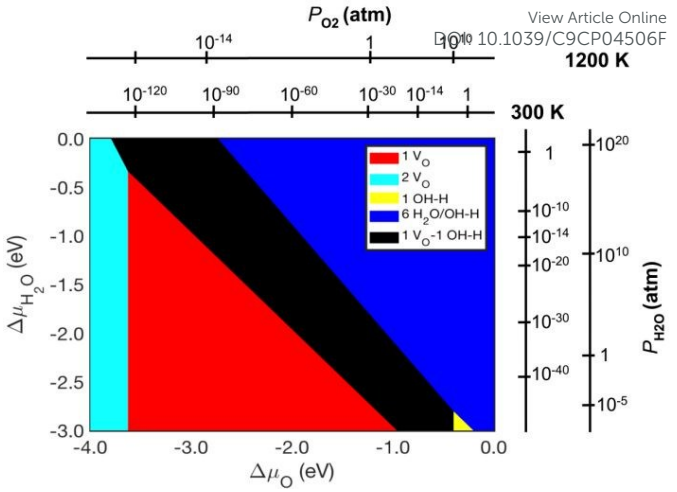


Figure 14. Interface energy (γ) as a function of the chemical potential of oxygen ($\Delta\mu_O$) and water ($\Delta\mu_{H2O}$) as defined in the methodology section. Top and bottom plots represent respectively the interface formed by TiN and a $TiO_2$ single layer. Here, the pristine surface is taken into account together with the low and highly reduced "dry" interfaces, and the low reduced and pristine interfaces in low and high water adsorbed concentration. The coloured areas represent the conditions where each interface is thermodynamically stable with respect to the other interface considered. Here OH-H indicates dissociated adsorption of water. We include two additional scales for each axis that represent the conversion in pressure (atm) of the chemical potential of the oxygen, calculated at T=300K and T=1200K.

As a first analysis, we compare the relative stability of the interface formed by a single $TiO_2$ layer on TiN. Here, we consider a "dry" interface model with the single oxygen vacancy and highly reduced with the multiple oxygen vacancies. Additionally, we consider the single oxygen vacancy and pristine interfaces with low and high water coverages of water. At regular ambient pressure, the pristine interface model fully covered with a mixture of molecular and dissociated water (Figure 9(b)) appears as the most stable configuration. At higher temperatures, the model with isolated water adsorbed in dissociated mode (Figure 5(b)) is stabilized at $P_{O2}$ and $P_{H2O}$ of 1 atm. We notice that the pristine interface is not stable under any conditions, and the highly reduced interface becomes stable only at very low values of both water and oxygen chemical potentials.

When considering the 2-layer $TiO_2$ either in **etched** or **slab** configuration, the analysis leads to a different conclusion. In this case, only three surfaces are stable within the considered range: pristine, highly hydrated and highly hydrated/highly reduced surfaces. The fully water covered stoichiometric models appear as the most stable structure at room temperature and pressure conditions. As discussed in the previous sections, our study considers the formation of O vacancies starting from a perfect

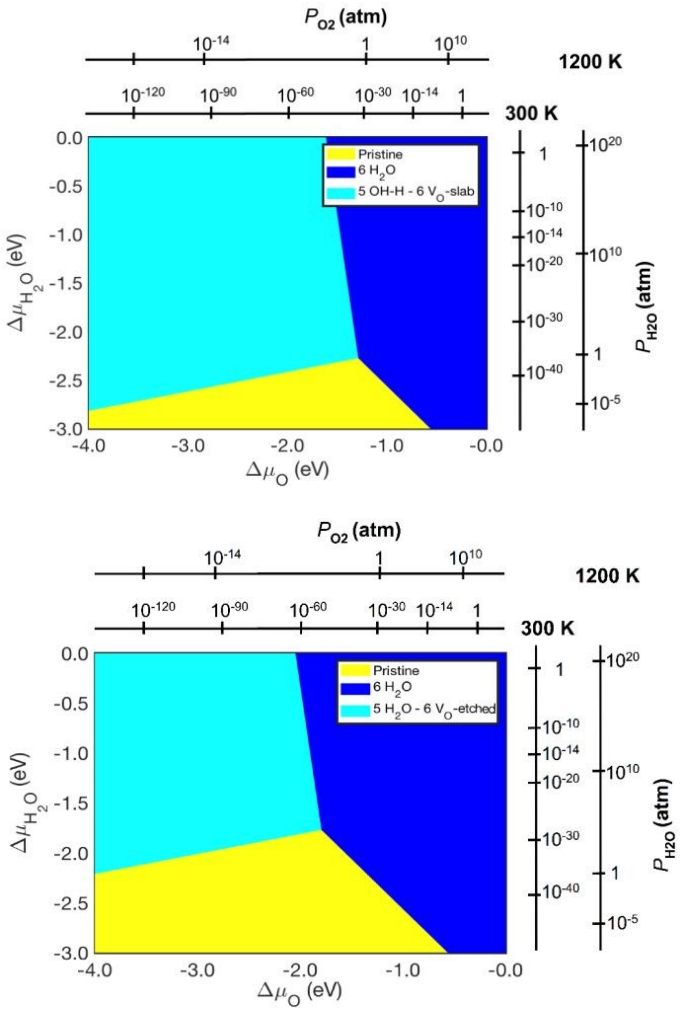


Figure 15. Interface energy (γ) as a function of the chemical potential of oxygen ($\Delta\mu_O$) and water ($\Delta\mu_{H2O}$) as defined in the methodology section. Top and bottom plots represent respectively the interface formed by TiN and a $TiO_2$ double layer in slab and etched configuration. Here, the pristine surface is taken into account together with the low and highly reduced "dry" interfaces, and the low reduced and pristine interfaces in low and high water adsorbed concentration. The coloured areas represent the conditions where each interface is thermodynamically stable with respect to the other interface considered. Here, $H_2O$ and OH-H indicate molecular and dissociated adsorption, respectively. We include two additional scales for each axis that represent the conversion in pressure (atm) of the chemical potential of the oxygen, calculated at T=300K and T=1200K.

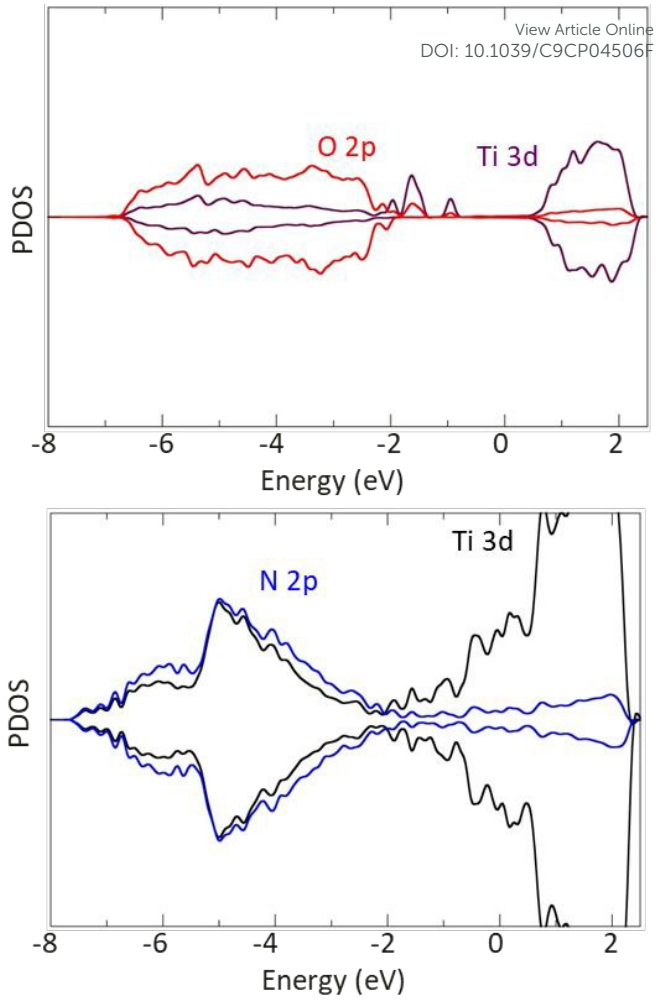


Figure 16. Spin-polarized Partial Density of States (PDOS) of 1-layer thick stoichiometric $TiO_2$-TiN interface. The graphs on the top and bottom panels represent $TiO_2$ and TiN PDOS. A legend with the contribution of each species is included in the graphs. Ti 3d electrons from TiN are represented with black lines, N 2p electrons in blue, Ti 3d electrons from $TiO_2$ in purple, and O 2p electrons from $TiO_2$ in red. The accumulated contribution of each species was considered for the total PDOS. The upper and lower halves of the graphs represent the spin-up and spin-down components respectively. The 0 eV energy stands for the Fermi level.

interface. However, defects are prone to form and remain trapped during oxide growth, and thus, non-stoichiometric oxide slabs can be stabilized at ambient conditions. The major difference between etched and slab configuration is that in etched conditions the highly hydrated interface is stable for a larger range of both $\Delta\mu_O$ and $\Delta\mu_{H2O}$.

### 3.5. Electronic structure of bare and hydrated $TiO_2$-TiN interface models

In this section, we discuss the electronic features of the different $TiO_2$-TiN interfaces and how these are affected by the adsorption of water. The Partial Density of States (PDOS) projected onto the Ti 3d and N 2p states from TiN, and the Ti 3d and O 2p states from $TiO_2$ for the 1-layer (stoichiometric) and 2-layer (stoichiometric and O-defective) $TiO_2$-TiN interfaces are presented in Figure 16 and Figure 17 respectively. The individual contribution of each element projected onto Ti 3d, N 2p and O 2p states are represented in different panels for the TiN and $TiO_2$ regions. A more detailed representation of the PDOS for all the bare (Figures S6-7) and hydrated (Figures S8-11) interfacial models in this study are included in the supporting information, whereas the most important features for selected cases are discussed below.

The distribution of the TiN PDOS represents the metallic character of this material due to the main contribution of Ti d-electrons to the states near the Fermi level ($E_F$). The PDOS shows Ti-N hybridization in for the states below -2 eV with a main peak centred at -5 eV, measured both with respect to $E_F$. These features are common to all the interfaces and do not

seem to be strongly affected by the thickness of the oxide or presence of defects in the oxide or the adsorption of water. Therefore, we will omit the description of the TiN in the successive discussion.

The $TiO_2$ PDOS shows the semiconductor character of this metal-oxide. The O 2p states dominate the states under the top edge of the valence band (VBM) with some Ti 3d contribution while the Ti 3d are the main responsible for the states at the bottom of the conduction band (CBM). We measured an energy gap between the valence and conduction bands of 2.7 eV in the 1-layer oxide slab and 2.6 eV for the 2-layer. These values are comparable to the main gap of the 4-layer thick oxide in a $TiO_2$-TiN interface of 2.5 eV,[40] calculated with an identical computational setup, and underestimated compared to the experimental value of $TiO_2$ gap of around 3 eV.[86] The underestimated values for the energy gap are generally observed in DFT and DFT+U simulations of rutile $TiO_2$ and do not affect the results presented in this work. The $Ti^{3+}$ states lay between the highest occupied states O 2p states and the lowest unoccupied Ti 3d states in $TiO_2$ as is commonly observed in reduced $TiO_2$[63] and other Ti-based metal-oxide interfacial systems like NiTi-$TiO_2$.[74] In the 1-layer model (Figure 16), the reduced $Ti^{3+}$ states occupy the states between VBM and -1.4 eV below $E_F$, which potentially reduces the energy gap to 1.9 eV. We observe also a small peak located in the mid-gap and centred at -1 eV from $E_F$. The formation of one oxygen vacancy in the 1-layer system does not produce significant changes in the PDOS, as can be observed in Figure S7.

The stoichiometric 2-layer oxide slab (Figure 17.a) exhibits an electronic energy gap of 2.6 eV with a mid-gap contribution from reduced $Ti^{3+}$ states lying between 0.5 eV above VBM and 1.3 eV below CBM. In the non-stoichiometric slabs, with $TiO_{1.75}$ composition, the $Ti^{3+}$ states occupy the states from VBM to about -1 eV below $E_F$. The presence of the $Ti^{3+}$ states contributes to a significant reduction of the energy gap, from 2.6 eV in the stoichiometric $TiO_2$-TiN model to 1.3 eV in the $TiO_{1.75}$-TiN systems.

The adsorption of water on the oxide slabs in $TiO_2$-TiN interfaces, presented in Figure 18 and Figures S9-S11, does not produce significant alterations in the $TiO_2$ PDOS. The PDOS for the 2-layer thick O-defective fully covered $TiO_{1.75}$-TiN interfaces model exhibit equivalent features for the **etched** and **slab** model interfaces. However, we observe clear differences in the PDOS between molecular and dissociative adsorption of water. In the interface with adsorbed $H_2O$ (Figure 18.a) the main O 2p states from $H_2O$ are distributed between -1.4 eV and -3.0 eV below the $TiO_2$ valence band, with several sharp O and H peaks in the region between -4.2 eV and -8.1 eV as measured from VBM. When water is dissociatively adsorbed, the hybridization between O 2p states from $TiO_2$ and OH is identified at higher energy states, with their main contribution between -0.6 eV and -2.4 eV below VBM. The O and H states from dissociated water are localized in a region between -4.9 eV and -7.9 eV below VBM. The most strongly bonded states (lowest energy) are more stable in the hydroxylated model compared to the model with molecular $H_2O$.

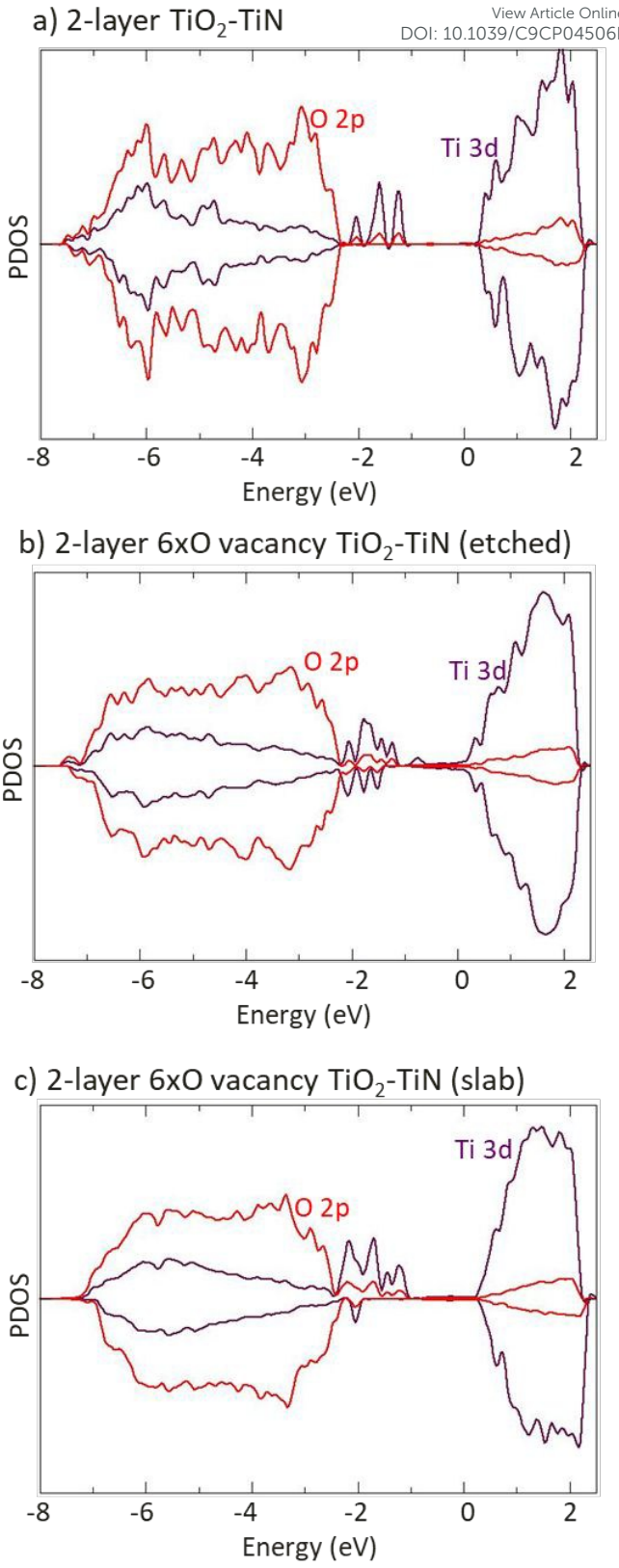


Figure 17. Spin-polarized partial Density of States (PDOS) of 2-layer thick $TiO_2$-TiN interfaces (a) stoichiometric, (b) etched model of $Ti_{1.75}$-TiN and (c) slab model of $Ti_{1.75}$-TiN.

View Article Online
DOI: 10.1039/C9CP04506F



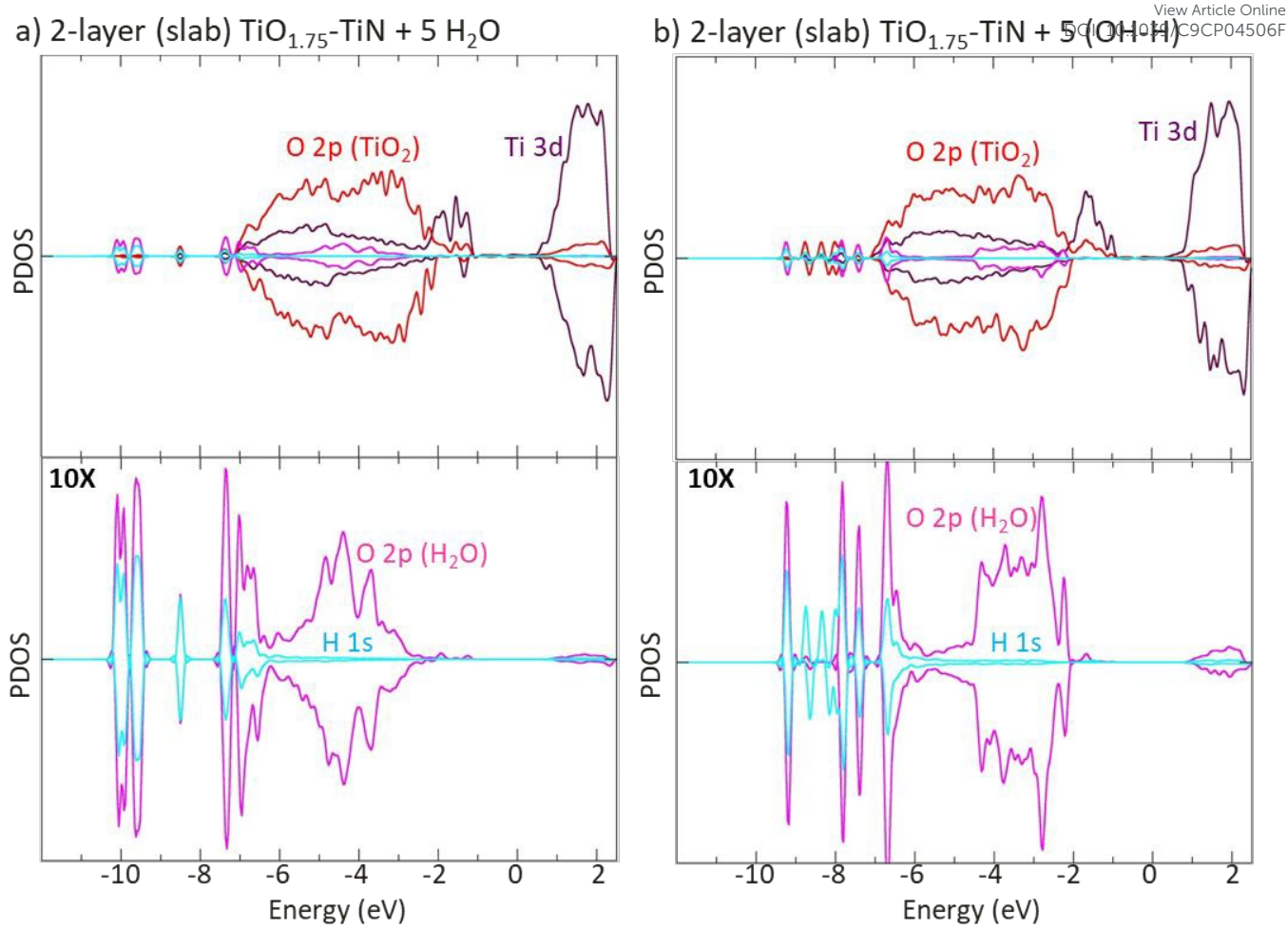


Figure 18. Spin-polarized Partial Density of States (PDOS) of $TiO_2$ for the fully covered slab model of $Ti_{1.75}$-TiN with (a) molecular $H_2O$ and (b) dissociated OH-H water. A legend with the contribution of each species is included in the graphs. Ti 3d electrons from TiN are represented with black lines, N 2p electrons in blue, Ti 3d electrons from $TiO_2$ in purple and O 2p electrons from $TiO_2$ in red. The accumulated contribution of each species was considered for the total PDOS. The individual contribution of O 2p states from water is shown under the main graphs and amplified by a factor of 10 with respect to the contribution of one single atom. The upper and lower halves of the graphs represent the spin-up and spin-down components, respectively. The 0 eV energy stands for the Fermi level.

The presence of several sharp peaks, that are localized at low energy states, denote the high stability of the adsorbed hydroxyls on the non-stoichiometric non-ordered $TiO_{1.75}$-TiN interface. In addition, the high concentration of reduced $Ti^{3+}$ states formed from charge transfer from the TiN substrate along with the formation of stable O vacancies leads to a significant reduction of the energy gap of this system compared to the stoichiometric slab, as discussed above.

## 5. Conclusions

We carried out a detailed first-principles study to describe the structural and electronic properties of ultra-thin $TiO_2$ layers (one and two-layer thick) supported on a rock-salt TiN surface model. These thinner $TiO_2$ layers are stabilized on the TiN surface through the formation of interfacial Ti – O bonds and show some notable differences compared to interfaces formed by thicker $TiO_2$ layers with TiN. Our Hubbard-corrected DFT+U calculations show charge transfer from the TiN towards the oxide, which leads to the formation of reduced $Ti^{3+}$ cations in $TiO_2$. The concentration of $Ti^{3+}$ cations is proportionally higher in the ultra-thin oxide, compared to interfacial models with thicker oxide layers.

The 1-layer model presents a strongly distorted oxide, due to the high concentration of reduced $Ti^{3+}$ atoms and the compression applied to $TiO_2$ to compensate the lattice mismatch with TiN. Our ab-initio thermodynamics calculations show the stability of oxygen vacancies in this interface for values of $\Delta\mu_0$ below -1.25 eV.

The oxide slab in the 2-layer thick $TiO_2$-TiN interfaces preserves the original symmetry of the rutile surface. The highly non-stoichiometric ($TiO_{1.75}$-TiN interface) **slab model**, generated by introducing six interfacial O vacancies in the 2-layer thick perfect interface, is highly distorted and it is more stable than the **etched oxide model**. The introduction of several vacancies in an already non-stoichiometric system becomes progressively more favourable, which suggests the stability of the highly non-stoichiometric interfaces, in line with our previous study on nitride-supported interfaces with thicker oxide [40].

We analysed the adsorption of molecular and dissociated water as a function of the surface coverage and the composition of the oxide-nitride interface. In our previous work, we showed that when water is adsorbed on the rutile surface of $TiO_2$–TiN interfaces with a 4-layer thick (bulk-like) oxide, the surface will be fully covered with molecular water at typical ambient conditions and this behaviour is similar to that observed on pure $TiO_2$ surfaces. However, it is well known that the film thickness is a key factor for the catalytic activity of oxides supported on a metal substrate, and the chemical activity of ultra-thin metal-oxide layers can be substantially enhanced compared to interfacial models with thicker oxide. One isolated water is dissociatively adsorbed on the stoichiometric and at the least distorted O-vacancy ultra-thin oxide slabs. At higher water coverages, our results suggest the likely stability of mixed environments with molecular $H_2O$ and hydroxyls on the 1-layer slab.

On the perfect 2-layer $TiO_2$ slab, 1ML of molecular $H_2O$ coverage is stabilized through the formation of H-bonds between adjacent water molecules. The resulting structure is similar to 1ML of $H_2O$ adsorbed on 4-layer thick oxide in $TiO_2$-TiN interfaces [40] or pure $TiO_2$. [55] On the other hand, the adsorption of a 1ML on the 2-layer thick non-ordered **slab model** presents the hydroxylated surface ($E_{ads}$ = -0.71 eV per $H_2O$) as the most energetically favoured model. This is mainly due to the lack of symmetry on the oxide surface, that penalises the stabilization of $H_2O$ avoiding the formation of H bonds with its neighbouring molecules.

The PDOS for the highly non-stoichiometric $TiO_{1.75}$-TiN systems shows the $Ti^{3+}$ states lying above the top of the valence band, which contributes to a significant reduction of the energy gap, from 2.6 eV in the stoichiometric $TiO_2$-TiN model to 1.3 eV in $TiO_{1.75}$-TiN.

Our DFT+U study of ultra-thin oxide in $TiO_2$–TiN interfaces indicate the preference for dissociated water on the disordered ultra-thin oxide slabs along with an important reduction of the electronic energy gap in the interfaces with highly non-stoichiometric oxides. Based on these analyses, we suggest the suitability of this interfacial system for photocatalytic water splitting applications. The main outcomes of this study can be also used as a guide to foster future applications for interfaces with ultra-thin oxide supported on a metallic substrate.

## Conflicts of interest

There are no conflicts to declare.

## Acknowledgements

This work was supported by the Environmental Protection Agency UisceSense project (W-2015-MS-21). J.J.G.M. and W.L. acknowledge financial support from the National Natural Science Foundation of China under Grant No. 31770777, the Postdoctoral Science Foundation of China under Grant No. 2018M643152 and the Startup Foundation for Peacock Talents, Shenzhen University. The authors wish to acknowledge the Paratera cloud server in China, DJEI/DES/SFI/HEA funded Irish Centre for High-End Computing (ICHEC) and the DECI-14 resource Bem based in Poland at WCSS with support from the PRACE aisbl for the provision of computational facilities and support.

## References

1. S. Zhang and W. Zhu, *Journal of Materials Processing Technology*, 1993, **39**, 165-177.
2. R. P. Van Hove, I. N. Sierevelt, B. J. van Royen and P. A. Nolte, *BioMed Research International*, 2015, **2015**, 485975/485971-485975/485979.
3. L. Toth, *Transition metal carbides and nitrides*, Academic Press, 1971.
4. H. O. Pierson, *Handbook of Refractory Carbides & Nitrides: Properties, Characteristics, Processing and Apps*, William Andrew, 1996.
5. F. Vaz, P. Machado, L. Rebouta, P. Cerqueira, P. Goudeau, J. Rivière, E. Alves, K. Pischow and J. De Rijk, *Surface and Coatings Technology*, 2003, **174**, 375-382.
6. L. I. Johansson, *Surface Science Reports*, 1995, **21**, 177-250.
7. P. Patsalas, N. Kalfagiannis and S. Kassavetis, *Materials*, 2015, **8**, 3128-3154.
8. T. Nakayama, H. Wake, K. Ozawa, N. Nakamura and T. Matsunaga, *Applied Microbiology and Biotechnology*, 1998, **50**, 502-508.
9. T. Nakayama, H. Wake, K. Ozawa, H. Kodama, N. Nakamura and T. Matsunaga, *Environmental Science & Technology*, 1998, **32**, 798-801.
10. P. Patsalas, N. Kalfagiannis, S. Kassavetis, G. Abadias, D. Bellas, C. Lekka, E. J. M. S. Lidorikis and E. R. Reports, 2018, **123**, 1-55.
11. P. J. Kelly and R. D. Arnell, *Vacuum*, 2000, **56**, 159-172.
12. G. Abadias, Y. Tse, P. Guérin and V. Pelosin, *Journal of Applied Physics*, 2006, **99**, 113519.
13. Y. Cheng, B. Tay, S. Lau, H. Kupfer and F. Richter, *Journal of Applied Physics*, 2002, **92**, 1845-1849.
14. G. Abadias, *Surface and Coatings Technology*, 2008, **202**, 2223-2235.
15. P. Jindal, A. Santhanam, U. Schleinkofer and A. Shuster, *International Journal of Refractory Metals and Hard Materials*, 1999, **17**, 163-170.
16. M. Nordin, M. Larsson and S. Hogmark, *Surface and Coatings Technology*, 1998, **106**, 234-241.
17. J. Wagner, C. Mitterer, M. Penoy, C. Michotte, W. Wallgram and M. Kathrein, *International Journal of Refractory Metals and Hard Materials*, 2008, **26**, 120-126.
18. H. Y. Lee, Y. H. Park and K. H. Ko, *Langmuir*, 2000, **16**, 7289-7293.
19. H. E. Rebenne and D. G. Bhat, *Surface and Coatings Technology*, 1994, **63**, 1-13.
20. K.-E. Elers, J. Winkler, K. Weeks and S. Marcus, *Journal of the Electrochemical society*, 2005, **152**, G589-G593.
21. J. Westlinder, T. Schram, L. Pantisano, E. Cartier, A. Kerber, G. Lujan, J. Olsson and G. Groeseneken, *IEEE Electron Device Letters*, 2003, **24**, 550-552.
22. C. Ernsberger, J. Nickerson, T. Smith, A. Miller and D. Banks, *Journal of Vacuum Science & Technology A: Vacuum, Surfaces, and Films*, 1986, **4**, 2784-2788.

23. X. Hou, K. C. Chou and M. Zhang, *International Journal of Applied Ceramic Technology*, 2010, **7**, 248-255.
24. M. Wittmer, J. Noser and H. Melchior, *Journal of Applied Physics*, 1981, **52**, 6659-6664.
25. L. Rebouta, F. Vaz, M. Andritschky and M. F. da Silva, *Surface and Coatings Technology*, 1995, **76**, 70-74.
26. I. Suni, D. Sigurd, K. Ho and M. A. Nicolet, *Journal of the Electrochemical Society*, 1983, **130**, 1210-1214.
27. J. Desmaison, P. Lefort and M. Billy, *Oxidation of Metals*, 1979, **13**, 505-517.
28. K. Uetani, H. Kajiyama, A. Takagi, I. Tokomoto, Y. Koizumi, K. Nose, Y. Ihara, A. Kato, K.-i. Onisawa and T. Minemura, *Materials Transactions*, 2001, **42**, 403-406.
29. S. Gwo, C. L. Yeh, P. F. Chen, Y. C. Chou, T. T. Chen, T. S. Chao, S. F. Hu and T. Y. Huang, *Applied Physics Letters*, 1999, **74**, 1090-1092.
30. H. Kawasaki, T. Ohshima, Y. Yagyu, Y. Suda, S. I. Khartsev and A. M. Grishin, *Journal of Physics: Conference Series*, 2008, **100**, 012038.
31. M. J. Jung, H. Y. Lee, J. G. Han, C.-K. Jung, J.-S. Moon and J.-H. Boo, *Journal of Vacuum Science & Technology B: Microelectronics and Nanometer Structures Processing, Measurement, and Phenomena*, 2005, **23**, 1826-1831.
32. S. Qamar, F. Lei, L. Liang, S. Gao, K. Liu, Y. Sun, W. Ni and Y. Xie, *Nano Energy*, 2016, **26**, 692-698.
33. Y. Zhao, Y. Zhao, R. Shi, B. Wang, G. I. Waterhouse, L. Z. Wu, C. H. Tung and T. Zhang, *Advanced Materials*, 2019, 1806482.
34. Z. Xie, X. Liu, P. Zhan, W. Wang and Z. Zhang, *AIP Advances*, 2013, **3**, 062129.
35. T. Morikawa, R. Asahi, T. Ohwaki, K. Aoki and Y. Taga, *Japanese Journal of Applied Physics*, 2001, **40**, L561.
36. C. Di Valentin, E. Finazzi, G. Pacchioni, A. Selloni, S. Livraghi, M. C. Paganini and E. Giamello, *Chemical Physics*, 2007, **339**, 44-56.
37. J. Zimmermann, M. W. Finnis and L. C. Ciacchi, *The Journal of Chemical Physics*, 2009, **130**, 134714/134711-134714/134711.
38. R. I. Hegde, R. W. Fiordalice, E. O. Travis and P. J. Tobin, *Journal of Vacuum Science & Technology B*, 1993, **11**, 1287-1296.
39. A. Moatti, R. Bayati and J. Narayan, *Acta Materialia*, 2016, **103**, 502-511.
40. J. J. Gutiérrez Moreno and M. Nolan, *ACS Applied Materials & Interfaces*, 2017, **9**, 38089-38100.
41. U. Diebold, *Surface Science Reports*, 2003, **48**, 53-229.
42. S. J. Bao, C. M. Li, J. F. Zang, X. Q. Cui, Y. Qiao and J. Guo, *Advanced Functional Materials*, 2008, **18**, 591-599.
43. H.-M. Lin, C.-H. Keng and C.-Y. Tung, *Nanostructured Materials*, 1997, **9**, 747-750.
44. J. Pan, C. Leygraf, D. Thierry and A. M. Ektessabi, *Journal of Biomedical Materials Research Part A*, 1997, **35**, 309-318.
45. K. Hashimoto, H. Irie and A. Fujishima, *Japanese Journal of Applied Physics*, 2005, **44**, 8269.
46. M. Geetha, A. Singh, R. Asokamani and A. Gogia, *Progress in Materials Science*, 2009, **54**, 397-425.
47. L. Graziani, E. Quagliarini, F. Bondioli and M. D'Orazio, *Building and Environment*, 2014, **71**, 193-203.
48. M. Lorenzetti, G. Bernardini, T. Luxbacher, A. Santucci, S. Kobe and S. Novak, *Biomedical Materials*, 2015, **10**, 045012.
49. R. Wang, K. Hashimoto, A. Fujishima, M. Chikuni, E. Kojima, A. Kitamura, M. Shimohigoshi and T. Watanabe, *Advanced Materials*, 1998, **10**, 135-138.
50. M. A. Henderson, *Surface Science Reports*, 2002, **46**, 1-308.
51. J. M. Pan, B. Maschhoff, U. Diebold and T. Madey, *Journal of Vacuum Science & Technology A: Vacuum, Surfaces, and Films*, 1992, **10**, 2470-2476.
52. N. Kumar, P. R. Kent, D. J. Wesolowski and J. D. Kubicki, *The Journal of Physical Chemistry C*, 2013, **117**, 23638-23644.
53. R. Schaub, P. Thostrup, N. Lopez, E. Lægsgaard, I. Stensgaard, J. K. Nørskov and F. Besenbacher, *Physical Review Letters*, 2001, **87**, 266104.
54. J. J. Gutiérrez Moreno, M. Fronzi, P. Lovera, A. O'Riordan and M. Nolan, *The Journal of Physical Chemistry C*, 2018, **122**, 15395-15408.
55. P. M. Kowalski, B. Meyer and D. Marx, *Physical Review B*, 2009, **79**, 115410.
56. J. Jung, H.-J. Shin, Y. Kim and M. Kawai, *Physical Review B*, 2010, **82**, 085413.
57. H.-J. Shin, J. Jung, K. Motobayashi, S. Yanagisawa, Y. Morikawa, Y. Kim and M. Kawai, *Nature Materials*, 2010, **9**, 442.
58. Z. Song, J. Fan and H. Xu, *Scientific Reports*, 2016, **6**, 22853.
59. P. E. Blöchl, *Physical Review B*, 1994, **50**, 17953-17979.
60. G. Kresse and D. Joubert, *Physical Review B*, 1999, **59**, 1758-1775.
61. J. P. Perdew and Y. Wang, *Physical Review B*, 1992, **45**, 13244-13249.
62. B. Himmetoglu, A. Floris, S. Gironcoli and M. Cococcioni, *International Journal of Quantum Chemistry*, 2014, **114**, 14-49.
63. B. J. Morgan and G. W. Watson, *Surface Science*, 2007, **601**, 5034-5041.
64. A. Iwaszuk and M. Nolan, *Physical Chemistry Chemical Physics*, 2011, **13**, 4963-4973.
65. J. Graciani, J. J. Plata, J. F. Sanz, P. Liu and J. A. Rodriguez, *The Journal of Chemical Physics*, 2010, **132**, 104703.
66. H. Cheng and A. Selloni, *The Journal of Chemical Physics*, 2009, **131**, 054703.
67. W. Tang, E. Sanville and G. Henkelman, *Journal of Physics: Condensed Matter*, 2009, **21**, 084204.
68. V. M. M. Marlo, *Physical Review B*, 2000, **62**.
69. H. Perron, C. Domain, J. Roques, R. Drot, E. Simoni and H. Catalette, *Theoretical Chemistry Accounts*, 2007, **117**, 565-574.
70. D. R. Stull and H. Prophet, *JANAF thermochemical tables*, DTIC Document, 1971.
71. M. Fronzi, S. Piccinin, B. Delley, E. Traversa and C. Stampfl, *Physical Chemistry Chemical Physics*, 2009, **11**, 9188-9199.
72. M. Fronzi, S. Piccinin, B. Delley, E. Traversa and C. Stampfl, *Rsc Advances*, 2014, **4**, 12245-12251.
73. S. Ikeda, J. Palleau, J. Torres, B. Chenevier, N. Bourhila and R. Madar, *Journal of Applied Physics*, 1999, **86**, 2300-2306.
74. M. Nolan and S. A. Tofail, *Physical Chemistry Chemical Physics*, 2010, **12**, 9742-9750.
75. N. Seriani, C. Pinilla and Y. J. T. J. o. P. C. C. Crespo, 2015, **119**, 6696-6702.
76. L. Szabová, M. F. Camellone, M. Huang, V. Matolín and S. Fabris, *The Journal of Chemical Physics*, 2010, **133**, 234705.
77. Z. Yang, Z. Lu and G. Luo, *Physical Review B*, 2007, **76**, 075421.

Physical Chemistry Chemical Physics ARTICLE

View Article Online
DOI: 10.1039/C9CP04506F

78. P. Luches, F. Pagliuca, S. Valeri, F. Illas, G. Preda and G. J. T. J. o. P. C. C. Pacchioni, 2011, **116**, 1122-1132.
79. Y. Sugizaki, K. Ozawa and K. Edamoto, *Japanese Journal of Applied Physics*, 2017, **56**, 085501.
80. A. C. Papageorgiou, G. Cabailh, Q. Chen, A. Resta, E. Lundgren, J. N. Andersen and G. Thornton, *The Journal of Physical Chemistry C*, 2007, **111**, 7704-7710.
81. X. Pan, M.-Q. Yang, X. Fu, N. Zhang and Y.-J. Xu, *Nanoscale*, 2013, **5**, 3601-3614.
82. G. Mattioli, F. Filippone, P. Alippi and A. A. Bonapasta, *Physical Review B*, 2008, **78**, 241201.
83. J. J. Gutiérrez Moreno, DOI: http://dx.doi.org/10.17172/NOMAD/2017.09.22-1.
84. S. Wendt, R. Schaub, J. Matthiesen, E. K. Vestergaard, E. Wahlström, M. D. Rasmussen, P. Thostrup, L. Molina, E. Lægsgaard and I. Stensgaard, *Surface Science*, 2005, **598**, 226-245.
85. H. Perron, J. Vandenborre, C. Domain, R. Drot, J. Roques, E. Simoni, J. J. Ehrhardt and H. Catalette, *Surface Science*, 2007, **601**, 518-527.
86. A. Amtout and R. Leonelli, *Physical Review B*, 1995, **51**, 6842-6851.

View Article Online
DOI: 10.1039/C9CP04506F



Water adsorbs dissociatively on O-defective ultra-thin $TiO_{1.75}$ supported on TiN. The $Ti^{3+}$ states reduce the energy gap compared to $TiO_2$.